NUMERICAL ANALYSIS OF THE EFFECT OF THE PRE-EXISTING CRACK OPENING ON THE DIRECTION OF THE SECONDARY CRACK PROPAGATION

by

Mingzhou Li

B.S., Nanjing Forestry University, 2015

Submitted to the Graduate Faculty of

Swanson School of Engineering in partial fulfillment

of the requirements for the degree of

Master of Science

University of Pittsburgh

2017

UNIVERSITY OF PITTSBURGH

SWANSON SCHOOL OF ENGINEERING

This thesis was presented

by

Mingzhou Li

It was defended on

March 31, 2017

and approved by

Luis E. Vallejo, Ph.D., Professor,

Departmental of Civil and Environmental Engineering

Julie M. Vandenbossche, Ph.D., Associate Professor,

Departmental of Civil and Environmental Engineering

Anthony T. Iannacchione, Ph.D., Associate Professor,

Departmental of Civil and Environmental Engineering

Thesis Advisor: Luis E. Vallejo, Ph.D., Professor,

Departmental of Civil and Environmental Engineering

NUMERICAL ANALYSIS OF THE EFFECT OF PRE-EXISTING CRACK OPENING ON THE DIRECTION OF SECONDARY CRACK PROPAGATION

Mingzhou Li, M.S.

University of Pittsburgh, 2017

This study involves an analysis of the development and direction of secondary crack propagation starting from openings of different shapes located in brittle prismatic samples subjected to either uniaxial compression or direct shear stress conditions. The findings from the study were then used to understand how notches (cracks) located at the toe of slopes made of brittle materials influence their failure. For the first part of the study, a theoretical analysis that uses closed form solutions, linear elastic fracture mechanics (LEFM) and a numerical analysis that uses a finite element software (ABAQUS) were conducted to understand how the degree of curvature of circular and elliptical openings develops critical stresses that were the locations of the failure of the openings. The theoretical and numerical analysis established that the degree of curvature of the openings had a tremendous influence on where the secondary cracks developed. For the case of the elliptical samples, the attitude of the ellipse also had an influence on how the secondary cracks extend.

For the case of the rock slopes with a notch (crack) at their toe, an extended finite element method (XFEM) based on linear elastic fracture mechanics (LEFM) theory was utilized to model the secondary crack propagation that takes place from the tip of the notch subjected to gravity induced compression and gravity induced lateral pressure. The analysis that used XFEM established that the ratio between the shear stress acting parallel to the axis of the toe crack, and

the vertical overburden compression normal to the axis of the notch had a marked influence on how the secondary cracks developed from the notch. If the ratio was less than one, the secondary crack developed at angles greater than 90° with respect to the crack axis. If the ratio was equal to one, the secondary crack developed exactly at 90°. If ratio was greater than one, the secondary crack was inclined at angles less than 90°. XEFM study also indicated that the opening of the notch has also an influence on the angle of secondary crack propagation from the tip of the notch.

TABLE OF CONTENTS

LIST OF TABLES

LIST OF FIGURES

PREFACE

I would like to acknowledge Professor Luis E. Vallejo for providing me the opportunity to conduct this research. His patient and professional guidance gave me plenty of useful advice not only in the research but also in my future development. In addition, Dr. Yu, Mr. Zhiqiang Lai and Mr. Huaizhong Liu gave me great support in using ABAQUS for the data analysis.

Also I would like to thank my parents and my girlfriend, Yunhan Jiang for their support during these two years.

1.0 INTRODUCTION AND LITERATURE REVIEW

1.1 MOTIVATION

In coastal area, erosion usually happens at the toe of the slope in the form of notch [1]. Wave action is the primary reason for this phenomenon. Here are two examples of a slope with a notch at its toe. Under the lateral and vertical load induced by earth pressure, tensile failure happens in the slope, as shown in Fig. 1.1. When the wave acts on the toe region of the slope, normal and shear force act on the face of the bluff. Material of the slope is removed from the toe of the bluff during this wash out process, as shown in Fig. 1.2. What we concern is the influence of the initial notch opening on the direction of the secondary crack propagation. Besides, considering the different history of loading on the earth, the lateral earth pressure would be different. The vertical earth pressure should be constant since that the gravity of the earth above the crack will not change generally. Hence, the ratio of the shear and normal stress induced from earth pressure also differs in real case. The influence of the variation of this ratio on the secondary crack propagation is also investigated in this study.

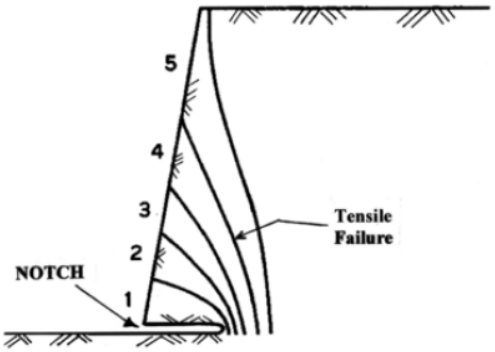

Figure 1.1. Progression of toe failures from an open toe notch in a soil slope in Vicksburgh, Mississippi [2]

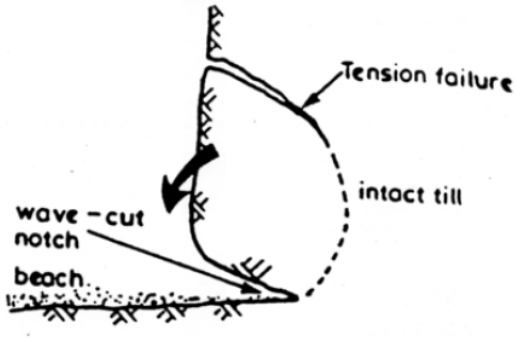

Figure 1.2. A wave induced notch and a notch induced failure in a coastal slope located in Aldbrough, England [3][4]

Before this, two tests are conducted on the prismatic brittle samples with different shape of opening. The objective of these two tests is to validate the accuracy of FEM in simulating the crack propagation in brittle material under mixed mode of loading. Two methods, finite element method (FEM) and linear elastic fracture mechanics (LEFM), are utilized in the validation tests as well as the notch study.

1.2 LINEAR ELASTIC FRACTURE MECHANICS

Linear elastic fracture mechanics (LEFM) is the fundamental theory of fracture, which began with experimental work by Griffith [1] [6] regarding the strength of glass and was then expended by Irwin [7][8] and Rice [9].

LEFM is a highly simplified, yet sophisticated, theory dealing with sharp cracks in elastic bodies. LEFM is applicable as long as one key condition met. A basic ideal situation is analyzed in LEFM in which all the material is elastic except in a vanishingly small region at the inelastic crack tip. The stresses near the crack tip are so high that the region becomes inelastic. Nevertheless, if the size of this inelastic zone is small enough relative to the dimensions of the whole domain, the nonlinear behavior induced within this region can be limited and then LEFM can be verified and utilized.

This chapter introduces certain studies in which LEFM has been applied to problems within geotechnical engineering. First, essential features of LEFM are discussed in order to demonstrate the parameters and criteria which are important in simulations. Second, the analytical solutions to the stress at holes and a sharp crack are summarized.

1.2.1 Fracture mechanics approach

Before we start introducing linear fracture mechanics as they apply to specific cases, it is useful to review Griffith's experimental work on the tensile strength of glass [1]. Griffith found that specific characteristics of the component had a significant influence on the tensile strength of the material. He also noticed that the inherent material property is not the only factor that determines the variability in tensile strength. If the material contains certain flaws, the common design approach

based on the criteria of material's strength is not applicable anymore because the stress at the stress at the tip of the sharp crack is infinitely high no matter how small the load is. Fracture mechanics approach should be utilized in this case because it takes the presence of flaw within the body into consideration.

Griffith supposed that solid surfaces are characterized by surface tension, in a manner analogous to liquids. Based on this hypothesis, a crack propagates or the surface area is going to increase as soon as the energy provided by surface tension is less than that introduced as a result of the external loads or internal released. In other words, it is necessary that the input energy rate exceeds the dissipated plastic energy, an energy balance equation which can be written as

$$\frac{\partial W}{\partial a} = \frac{\partial U_s^e}{\partial a} + \frac{\partial U_s^p}{\partial a} + \frac{\partial U_\Gamma}{\partial a} \tag{1.1}$$

in which W denotes the work done by the external force, U_s^e and U_s^p represents the elastic and plastic parts of the total strain energy respectively, and U_Γ denotes the surface tension energy.

We can rewrite Eq. (1.1) with respect to the potential energy $\Pi = U_s^e - W$, that is,

$$-\frac{\partial \Pi}{\partial a} = \frac{\partial U_s^p}{\partial a} + \frac{\partial U_\Gamma}{\partial a} \tag{1.2}$$

which represents a stability criterion for the crack and states that the rate at which the potential energy is released must equal the rate that energy is dissipated in plastic deformation and crack propagation. In addition, Irwin demonstrated that rate of input energy is independent of the load application modalities, but is related to the rate of strain energy release when the crack propagates in a unit length.

In the case of brittle materials, the plastic term U_s^p vanishes, and the energy balance shown above can be rewritten as

$$\frac{\partial U_\Gamma}{\partial a} + \frac{\partial \Pi}{\partial a} = 0 \tag{1.3}$$

The crack growth stability may be assessed by simply considering the second derivative of $(\Pi + U_\Gamma)$; the crack propagation will be either unstable or stable, depending on whether the energy at equilibrium assumes its maximum or minimum value, respectively. This can be described as the following fracture propagation criterion defined by

$$\frac{\partial^2(\Pi + U_\Gamma)}{\partial a^2} = \begin{cases} < 0 & \text{unstable fracture} \\ = 0 & \text{stable fracture} \\ > 0 & \text{neutral equilisbium} \end{cases} \tag{1.4}$$

The strain energy release rate $\mathcal{G}$ can be expressed as

$$\mathcal{G} = -\frac{\partial \Pi}{\partial a} = 2\gamma_s \tag{1.5}$$

where γ_s is the surface energy which should be doubled, given the existence of two cracked surfaces.

Substituting Eq. (1.5) in Eq. (1.3), the energy balance can be rewritten with respect to the energy release rate $\mathcal{G}$ as

$$\mathcal{G} - \frac{\partial U_\Gamma}{\partial a} = 0 \tag{1.6}$$

Griffith provided the theoretical solution for the strain energy in the case of an infinite plate subjected to uniaxial tension with a central crack of length $2a$, as shown in Fig. 1.3, below, which demonstrates that the strain energy needed for the crack to propagate is equal to the energy needed for the crack to close under the action of the stress, which can be described as

$$\Pi = 4\int_0^a \sigma u_y(x)dx = \frac{\pi\sigma^2 a^2}{2E'} \quad \Longrightarrow \quad \mathcal{G} = \frac{\pi a \sigma^2}{E'} \tag{1.7}$$

where E', an important parameter in fracture mechanics, is given by

$$E' = \begin{cases} E & \text{Plane stress} \\ \dfrac{E}{1-\upsilon^2} & \text{Plane strain} \end{cases} \tag{1.8}$$

in which E denotes the Young's modulus and υ the Poisson's ratio.

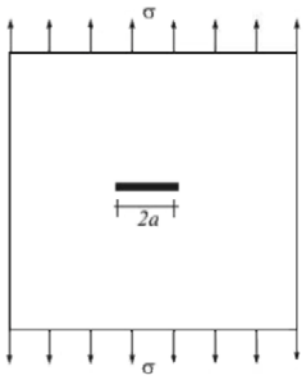

Figure 1.3. Infinite plate with central crack of length 2a, subjected to a uniaxial stress state [1]

Combining Eq. 1.5 and Eq. 1.7., we can calculate the relationship between the critical stress and the surface energy as

$$\sigma_{cr} = \sqrt{\frac{2E'\gamma_s}{\pi a}} \tag{1.9}$$

Griffith theory gives the energy balance criterion with approach of LEFM that enables us to identify whether the crack propagation is stable. In this way, LEFM is a useful tool for analyzing and predicting crack propagation and for characterizing the fracture extension rate.

1.2.2 Stress intensity factor and energy release rate

Griffith established the energy balance relationship which can be used to identify whether the crack propagation is stable or not, however, there is no general term that describes the stress state at the

crack tip. Irwin [7] recognized that all the stress equations contain the same expression $\sigma_{cr}\sqrt{\pi a}$, which can describe the severity of the crack tip comprehensively with the combination of σ_{cr} and a. Then stress intensity factor is given as

$$K_{\mathrm{IC}} = \sigma_{cr}\sqrt{\pi a} \tag{1.10}$$

By now combining Eq. 1.5, Eq. 1.9, and Eq. 1.10, Irwin obtained one important relationship in LEFM, between stress intensity factor K_{I} and energy release rate $\mathcal{G}$ in a more general way as

$$K_{\mathrm{I}} = \sqrt{E'\mathcal{G}} \tag{1.11}$$

At this time, it is worthwhile to provide a concise description of the crack behavior as shown in Fig. 1.4. A crack may be provoke by extremely complicated load conditions, however, these conditions can be considered as a combination of three cases of loading conditions or crack openings modes:

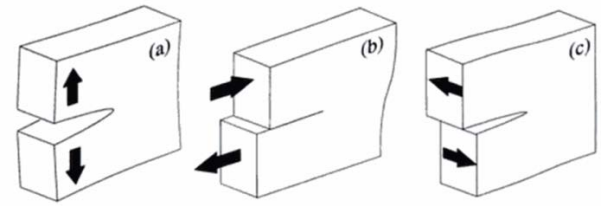

Figure 1.4. Sketches of crack opening modes: (a) Mode I or pure opening mode; (b) Mode II or in-plane shear mode; (c) Mode III or anti-plane shear mode [10]

- Mode I, characterized as a symmetric crack opening happens with respect to the crack plane, also termed as pure opening;
- Mode II, denoted as an antisymmetric separation of crack surfaces due to relative displacement in crack propagation direction, that is, normal to the crack front;

- Mode III, defined as a separation due to relative displacement in the direction tangential to the crack front.

Stress intensity factor is one of the most fundamental and useful parameters in all of fracture mechanics, not only the LEFM. It describes the stress state at the crack tip and can be utilized to establish the fracture criterion.

1.2.3 Stress concentration and distribution around holes

Theoretical study for stress concentrations around excavations are originated by Kirsch [11] in his linear elastic solution for stresses around a circular excavation in a finite plate under uniaxial compression, which is corresponded to the loading condition in the first test of this study. Began with this initial solution, more theoretical analysis of different loading condition is further investigated. The solution of stress around the hole under loading condition including shear stress is obtained in this study. In the case of excavation with other geometry like ellipse, Jaeger and Cook gave the solutions for the stress distribution expressed in respect of elliptical curvilinear co-ordinates.

1.2.3.1 Circular excavation

The solution for the stress at a circular excavation originally given by Kirsch [11] is for the case under uniaxial tension. Denoting with σ_∞ the remote stress, with a the radius of the circular excavation, with r the radial coordinate, with θ the angle counter clockwise from the line which aligns with the remote loading direction, the stress around the circular excavation in Fig. 1.5 is depicted as

$$\sigma_{rr} = \frac{P}{2}\left\{\left[1 - \left(\frac{a}{r}\right)^2\right] + \left[1 - 4\left(\frac{a}{r}\right)^2 + 3\left(\frac{a}{r}\right)^4\right]\cos 2\theta\right\}$$

$$\sigma_{\theta\theta} = \frac{P}{2}\left\{\left[1 + \left(\frac{a}{r}\right)^2\right] + \left[1 + 3\left(\frac{a}{r}\right)^4\right]\cos 2\theta\right\} \tag{1.12}$$

$$\tau_{r\theta} = -\frac{P}{2}\left[1 + 2\left(\frac{a}{r}\right)^2 - 3\left(\frac{a}{r}\right)^4\right]\sin 2\theta$$

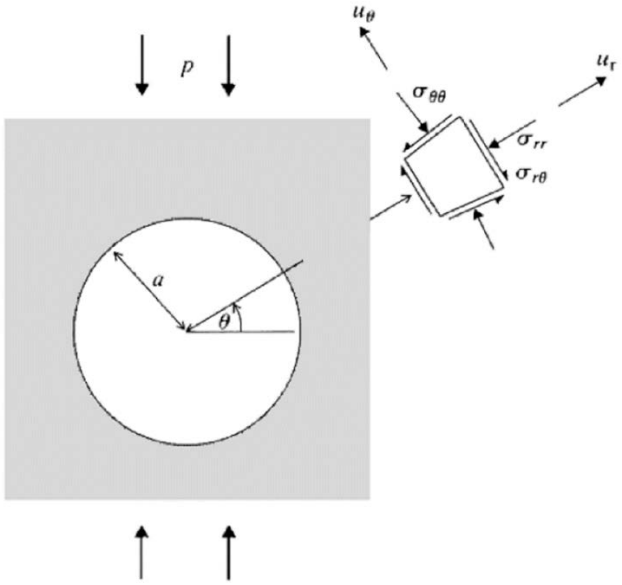

Figure 1.5. Stress analysis around the circular excavation under uniaxial stress field [13]

Through superimposing the induced stresses in respect of vertical stress p and horizontal stress Kp, the solution for the stress around the circular excavation subject to biaxial stress as shown in Fig. 1.6 is derived as

$$\sigma_{rr} = \frac{P}{2}\left\{(1+K)\left[1 - \left(\frac{a}{r}\right)^2\right] + (1-K)\left[1 - 4\left(\frac{a}{r}\right)^2 + 3\left(\frac{a}{r}\right)^4\right]\cos 2\theta\right\}$$

$$\sigma_{\theta\theta} = \frac{P}{2}\left\{(1+K)\left[1 + \left(\frac{a}{r}\right)^2\right] + (1-K)\left[1 + 3\left(\frac{a}{r}\right)^4\right]\cos 2\theta\right\} \tag{1.13}$$

$$\tau_{r\theta} = -\frac{P}{2}(1-K)\left[1+2\left(\frac{a}{r}\right)^2 - 3\left(\frac{a}{r}\right)^4\right]\sin 2\theta$$

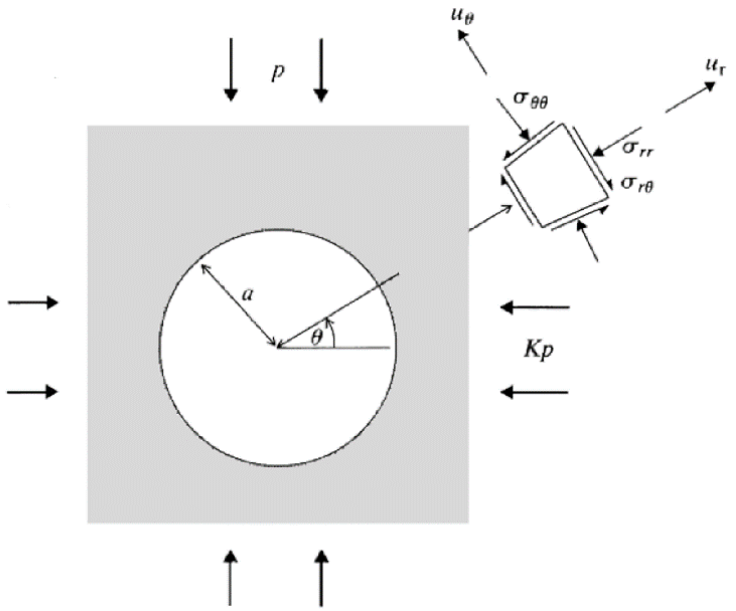

Figure 1.6. Stress analysis around the circular excavation under biaxial compression field [13]

Substituting $r = a$ in Eq. 1.13, we can derive the stresses on the excavation boundary as

$$\sigma_{\theta\theta} = p[(1+K) + 2(1-K)\cos 2\theta]$$
$$\sigma_{rr} = 0 \qquad (1.14)$$
$$\sigma_{r\theta} = 0$$

Eq. 1.14 depicts the state of stress on the boundary of a circular excavation under biaxial stress field. Clearly, for the element around the excavation boundary, only tangential stress exists since that there is no force loading on the boundary surface. When $K < 1$, i.e., the lateral stress is less than the vertical force, the maximum and minimum boundary stresses occur at the side wall ($\theta = 0$) and crown ($\theta = \pi/2$) of the excavation given by Brady & Brown [13] as

at point A: $\theta = 0$, $\sigma_{\theta\theta,A} = \sigma_A = p(3 - K)$

at point B: $\theta = \pi/2$, $\sigma_{\theta\theta,B} = \sigma_B = p(3K - 1)$ (1.15)

These equations give the maximum and minimum stresses under biaxial stress field, however, they are also applicable for the case of the uniaxial stress field as soon as we substitute $K = 0$ in, and the maximum and minimum stresses under uniaxial stress field is depicted as

$$\sigma_A = 3p$$
$$\sigma_B = -p \quad (1.16)$$

For the case with shear around the excavation, in order to use Equations derived above, the stress field is transferred using Mohr's Circle. The resulting stresses can be derived as

$$p = \sigma_1 = \frac{\sigma_y + \sigma_x}{2} + \sqrt{\left(\frac{\sigma_y - \sigma_x}{2}\right)^2 + {\tau_{xy}}^2}$$
$$Kp = \sigma_3 = \frac{\sigma_y + \sigma_x}{2} - \sqrt{\left(\frac{\sigma_y - \sigma_x}{2}\right)^2 + {\tau_{xy}}^2} \quad (1.17)$$

1.2.3.2 Elliptical excavation

Solutions for the stress distribution in this case are referred to Poulos and Davis [14] and Jaeger and Cook [12]. Elliptical curvilinear coordinates are utilized to present the solutions. Heok, E., and J. W. Bray [15] gave a solution to simplify the calculation of stress at the elliptical opening boundary. The problem geometry is depicted in Fig. 1.7. The global *x* axis is parallel to the direction of lateral stress Kp, and the local x_1 axis for the opening is defined by an axis of the ellipse. The width, W, of the ellipse is measured in the direction of x_1 axis, and the height, H, in the direction of the local z_1 axis. The attitude of the elliptical excavation in the biaxial stress field

is depicted by the angle between the local and global axes. The boundary stresses around an elliptical opening with axes inclined to the field stress directions are derived as

$$\sigma = \frac{p}{2q}\{(1+K)[(1+q^2)+(1-q^2)cos2(\theta-\beta)] - (1-K)[(1+q)^2\cos 2\theta + (1-q)^2\cos 2\beta]\} \tag{1.18}$$

where p represents the vertical force, K represents the ratio between the vertical and lateral stress, q represents the ratio between width and height of the elliptical opening, θ represents the angle counter clockwise from the local x_1 axis, and β represents the angle from the global x axis to the local x_1 axis.

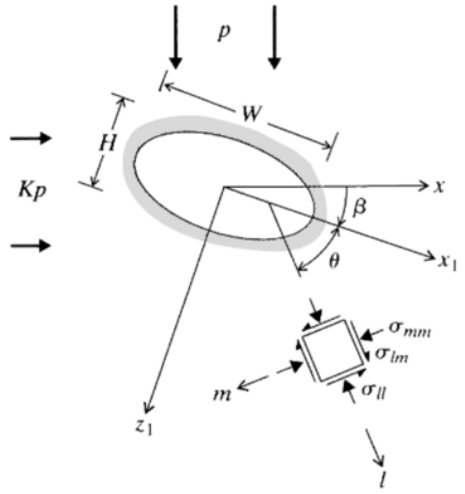

Figure 1.7. Stress analysis around the inclined elliptical excavation under biaxial compression field [13]

For the elliptical opening of which the local x_1 axis is parallel to the global x axis (see Fig. 1.8), that is, $\beta = 0$, Eq. 1.18 can be rewritten as

$$\sigma = \frac{p}{2q}\{(1+K)[(1+q^2)+(1-q^2)cos2\theta] - (1-K)[(1+q)^2\cos 2\theta + (1-q)^2]\} \tag{1.19}$$

Substituting $\theta = 0$ and $\theta = \pi/2$ into Eq. 1.19 respectively, sidewall and crown boundary stresses can be derived as

$$\sigma_A = p(1 - K + 2q)$$
$$\sigma_B = p(K - 1 + 2K/q) \tag{1.20}$$

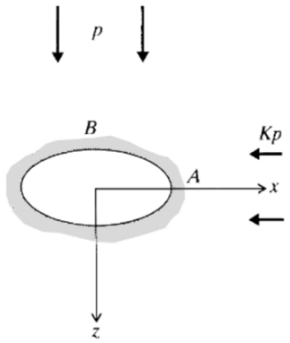

Figure 1.8. Stress analysis around the horizontal elliptical excavation under biaxial compression field [13]

1.2.4 Stress field at a crack tip

The maximum tangential stress criterion is originally developed by Erdogan and Sih [16], giving solutions to depict the stress field around a crack tip. It is applied by Luis E. Vallejo [17] to identify when the crack propagates as well as the direction of the secondary crack propagation

Denoted with r the distance from the crack tip, θ the angle that radius r makes with the $\sigma_{\theta\theta}$ the tangential stress, σ_{rr} the radial stress, and $\tau_{r\theta}$ the shear stress, stresses around a crack tip [18] shown in Fig. 1.9 can be obtained as

$$\sigma_{\theta\theta} = \frac{1}{\sqrt{2\pi r}} cos\frac{\theta}{2}\left[K_{\mathrm{I}} cos^2\frac{\theta}{2} - \frac{3}{2}K_{\mathrm{II}} sin\theta\right] \tag{1.21}$$

$$\sigma_{rr} = \frac{1}{\sqrt{2\pi r}} cos\frac{\theta}{2}\left[K_{\mathrm{I}}(1 + sin^2\frac{\theta}{2}) + \frac{3}{2}K_{\mathrm{II}}sin\theta - 2K_{\mathrm{II}}tan\frac{\theta}{2}\right]$$

$$\tau_{r\theta} = \frac{1}{\sqrt{2\pi r}} cos\frac{\theta}{2}[K_{\mathrm{I}}sin\theta + K_{\mathrm{II}}(3cos\theta - 1)]$$

where K_{I} and K_{II} are stress intensity factors under loading of Mode I and Mode II shown in Fig. 1.4 are given as

$$K_{\mathrm{I}} = 1.1215\ \sigma_n(\pi c)^{1/2}$$
$$K_{\mathrm{II}} = 1.1215\ \tau\ (\pi c)^{1/2} \tag{1.22}$$

where σ_n is the normal stress on the plane of opening crack, τ is the shear stress on the plane of opening crack, and c is half of the length of a whole crack, in this case, is just the length of the opening crack in Fig. 1.9, which is considered as one half of a whole crack.

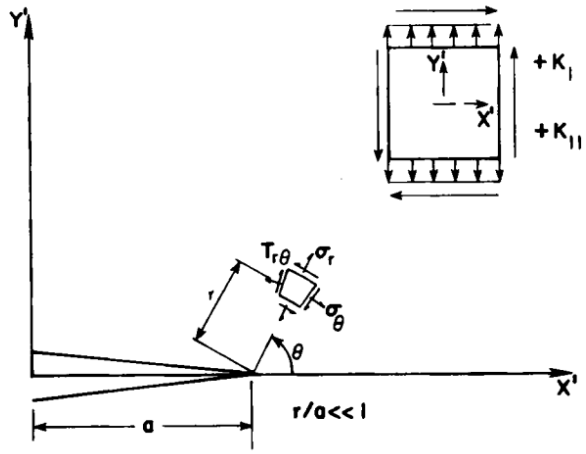

Figure 1.9. Crack tip stresses and system of reference [18]

Erdrogan and Sih [16] have proposed the hypothesis that crack extension happens in the direction in which tangential stress $\sigma_{\theta\theta}$ reaches its maximum value. Furthermore, the direction of

the propagation is aligned to a radius direction from the crack tip and this radius direction is perpendicular to the maximum tangential stress. Hence, the angle of direction of crack propagation, α is obtained as

$$\frac{d\sigma_{\theta\theta}}{d\theta} = 0 \quad at \quad \theta = \alpha \tag{1.23}$$

Substituting Eq. 1.21 and 1.22 into Eq. 1.23,

$$K_{\mathrm{I}} sin\alpha + K_{\mathrm{II}}(3cos\alpha - 1) = 0 \tag{1.24}$$

This method is for the case in which the crack is open. For the case of closed crack, the stress intensity factor for Mode I is zero, Eq. 1.24 can be rewritten as

$$3\cos\alpha - 1 = 0 \tag{1.25}$$

The theoretical value of the angle of crack propagation, α can be derived in the equation above and is equal to 70.5 degrees.

LEFM has been proved to deal with stress analysis around a crack tip in brittle material. In addition, the direction of secondary crack propagation can be derived through the maximum tangential fracture criterion based on LEFM.

1.2.5 Fracture criterion in LEFM

In the last chapter, we derived the stress intensity factor which allowed us to discuss fracture criterion. For Mode I, the crack will propagate when this stress intensity factor reaches a certain critical value K_{IC}, denoted with fracture toughness. According to Eq. 1.11, K_{IC} is related to the energy release rate at the critical state as

$$K_{\mathrm{IC}} = \sqrt{E'\mathcal{G}_{cr}} \tag{1.26}$$

with this definition, the local fracture criterion based on the stress intensity factor can be defined as

$$K_{\mathrm{I}} = \sqrt{E'\mathcal{G}} \begin{cases} < K_{\mathrm{IC}} & \text{No Crack Growth} \\ = K_{\mathrm{IC}} & \text{Quasi} - \text{static growth} \\ > K_{\mathrm{IC}} & \text{Dynamic growth} \end{cases} \tag{1.27}$$

For loading that are not only in Mode I (pure mode), identification of crack growth will be more complicated, the criterion must give not only the loading combination that provokes the fracture, but also the direction of the crack propagation.

Experiments show that under mixed mode loading, the crack will not propagate along a path which is align to the crack plane, but with an angle with respect to the crack plane. In this case, the direction of propagation is determined using the maximum tangential fracture criterion given by Erdogan and Sih [16] which has been illustrated in the last section.

1.3 EXTENDED FINITE ELEMENT METHOD

1.3.1 Finite Element Method

Here provided a brief introduction to the finite element method theory. Finite element method discretizes the region into a finite number of elements. For each element, approximate function is proposed based on the nodal variables. For a boundary value problem, only variables on the node of the boundaries are known, FEM is utilized to find the unknown variables on the other nodes.

There are certain variation methods, one of which is weak form Galerkin method. One key point in weak form Galerkin method is to obtain the weak form equations from the strong form

equations. In order to accomplish this, a strong form of governing equation, $g(x)$ should be expressed as a weighted integral, i.e.,

$$\int w(x)g(x)dx = 0 \tag{1.28}$$

In Galerkin method, shape functions, $N_i(x)$ are utilized to construct weight functions, $w(x)$. In addition, shape functions are also utilized to construct approximation $u(\mathrm{x})$ as

$$u(\mathrm{x}) = \sum_{i=1}^{n} N_i(x)u_i \tag{1.29}$$

where u_i is the displacement at node i. We can derive a final equation through integrating Eq. 1.28 and obtain the unknowns.

1.3.2 Extended Finite Element Method

Finite element method has been utilized in industry, however, simulating the crack propagation is still difficult due to the following reasons:

- The need to remesh the domain due to the modification of the mesh topology
- The difficulty of conforming the discretization corresponding to the evolving discontinuities where mesh must to be regenerated at each step
- The singularity must to be represented by an approximation

Over the last few decades, several approaches have been investigated to model crack problems. For example, quarter-point finite element[19] and enriched finite element [20] [21] have been combined with the high order isoparametric elements to represent the singularity at the crack tip. In addition, the dislocation method is investigated in order to model the branched crack problems [22] [23] [24]. An improved boundary collocation method is investigated to analyze the

stress around boundary of various geometry [25]. Element-free Galerkin method has been used to eliminate the part of the model constructed by approximation based on node, making it possible to simulate the crack propagation with arbitrary and complex path [26] [27] [28]. On the basis of all of these efforts to improve the finite element method, XFEM was created through use of enrichment technique. The motivation behind the extended finite element method was to find a method to simulate the discontinuity without remeshing the whole geometry. The essential idea of XFEM is to add an enrichment function, which is discontinuous, to the finite element approximation based on the unity of partition properties of the finite element method, thereby incorporating the discontinuous field and asymptotic field near the crack tip. This technique approximates the crack independent on the mesh so that there is no need to do the remesh.

XFEM was originated by enriching the finite element approximation created by Belytschko and Black [29]. They derived a discontinuous enrichment function and combined it with finite element approximation to represent the crack and allow the crack to propagate in an arbitrary direction. This method was completed by Dolbow et al. [30][31][32], who adapted an enrichment that includes the asymptotic near-tip field and a Heaviside function. The Heaviside function is a discontinuous jump function across the crack surface and is constant on each side of the crack (+1 on one side and -1 on the other). In addition, the mapping algorithm [28] is utilized to improve the enrichment technique.

Sukumar et al. [33][34] implemented XFEM to produce three-dimensional crack modeling, utilizing a discontinuous function to model the interior of the crack surface and the function from the two-dimensional asymptotic crack tip displacement field for the crack front enrichment. Belytschko et al. [35] unified the methodology for representing the discontinuities that are independent of mesh. They improved the method of constructing approximations for discontinuous

functions originally proposed by Belytschko and Black [29], Dolbow et al. [32], and Sukumar et al. [33][34].

1.3.2.1 Partition of unity enriched finite element method

XFEM is based on a partition of unity (PU) concept where a domain Ω is divided into over lapping sub-domains Ω_I, each of which is associated with a function $\phi_I(x)$ which is non-zero in Ω_I. Thus, PU in a domain can be represented as a set of functions which obey the following property

$$\sum_{I=1}^{N} \phi_I(x) = 1 \quad \text{in} \quad \Omega \tag{1.30}$$

The partition of unity finite element method provides a theoretical framework which is utilized in the XFEM. This property of a partition of unity can be utilized in XFEM and GFEM with any arbitrary function $\psi(x)$ represented as a product of the partition of unity functions with $\psi(x)$, that is, if we extend the methodology for any arbitrary function $\psi(x)$, but not for unity, Eq. 1.30 can be rewritten as

$$\sum_{I=1}^{N} \phi_I(x)\psi(x) = \psi(x) \quad \text{in} \quad \Omega \tag{1.31}$$

This is also the basic idea of constructing the approximation functions in Galerkin method of FEM:

$$\sum_{I=1}^{N} N_I(x)\psi(x) = \psi(x) \quad \text{in} \quad \Omega \tag{1.32}$$

where $N_I(x)$ also obeys the following property

$$\sum_{\mathrm{I}=1}^{N} N_{\mathrm{I}}(x) = 1 \quad \text{in} \quad \Omega \tag{1.33}$$

Furthermore, this approach can be utilized in the enrichment procedure, which can increase the order of a finite element approximation. In other words, the accuracy of the approximation can be improved by including a partition of unity framework in the framework of the isoparametric finite element discretization. This process is called enrichment. And the approximation including the enrichment function using partition of unity is then expressed as

$$u^h(x) = \sum_{\mathrm{I}=1}^{N} N_{\mathrm{I}}(x)\, u_I + \sum_{I=1}^{N} \sum_{J=1}^{M} N_{IJ}(x)\, \phi_{IJ}(x)\, t_{IJ} \tag{1.34}$$

where $\phi_{IJ}(x)$ are called the enrichment functions, t_{IJ} are the induced unknown nodal values resulting from enrichment, $N_{IJ}(x)$ are the shape functions corresponding to node IJ. As can be seen on the right side of the Equation, the functions in the first term approximate the general finite elements, and those in the second term approximate the enriched finite elements. Generally, $N_{IJ}(x)$ is equal to $N_{\mathrm{I}}(x)$ [36], so Eq. 1.34 can be combined and rewritten as

$$u^h(x) = \sum_{\mathrm{I}=1}^{N} N_{\mathrm{I}}(x) \left(u_I + \sum_{J=1}^{M} \phi_{IJ}(x)\, t_{IJ} \right) \tag{1.35}$$

At an enriched node I, considering the partition of unity property,

$$u^h(x_I) = \sum_{\mathrm{I}=1}^{N} N_{\mathrm{I}}(x_I) \left(u_I + \sum_{J=1}^{M} \phi_{IJ}(x_I)\, t_{IJ} \right) = u_I + \sum_{J=1}^{M} \phi_{IJ}(x_I)\, t_{IJ} \tag{1.36}$$

However, according to the interpolation at nodal point,

$$u^h(x_I) = u_I \tag{1.37}$$

Comparing Eq. 1.36 and Eq. 1.37, Eq. 1.35 can be modified as

$$u^h(x) = \sum_{\mathrm{I}=1}^{N} N_{\mathrm{I}}(x)\left\{u_I + \sum_{J=1}^{M}\left[\phi_{IJ}(x) - \phi_{IJ}(x_I)\right] t_{IJ}\right\} \tag{1.38}$$

An increase of the order of finite element discretization is achieved in the Generalized Finite Element Method (GFEM). In this method, the shape functions for the standard element and enriched element are different, then the equation above can be rewritten as

$$u^h(x) = \sum_{I=1}^{N} N_I(x)\, u_I + \sum_{I=1}^{N}\sum_{J=1}^{M} N'_J(x)\left[\phi_{IJ}(x) - \phi_{IJ}(x_I)\right] t_{IJ} \tag{1.39}$$

1.3.2.2 Enrichment functions for crack tip

The basic approach of XFEM is that the approximation can be enriched by adding enrichment functions and it is accomplished by using partition of unity, we will now apply this basic approach to modelling the domain with a crack.

Two-dimensional plane strain asymptotic crack tip field function

Before we start, it is necessary to introduce the crack-tip enrichment functions within the two-dimensional plane strain asymptotic near-tip field given by Belytschko and Black [29]. These four functions are originated from displacement field in LEFM theory and have been proved to be included within the span of the local crack tip radial coordinate system (r, θ):

$$\begin{aligned}\phi\ (\mathrm{x}) &= \{F_l(r,\theta)\}_{l=1}^{4} \\ &= \left\{\sqrt{r}\cos\left(\frac{\theta}{2}\right), \sqrt{r}\sin\left(\frac{\theta}{2}\right), \sqrt{r}\sin\left(\frac{\theta}{2}\right)\sin\theta\,, \sqrt{r}\cos\left(\frac{\theta}{2}\right)\right\}\end{aligned} \tag{1.40}$$

Four different degrees of freedom for each direction corresponding to each direction of each node are added to the initial degrees of freedom associated with the standard finite element discretization. Among these four functions, only the second term $\sqrt{r}\sin\left(\frac{\theta}{2}\right)$ is a discontinuous

function with respect to the crack surface. Thus, the second function simulates the discontinuity property and the other three improve the simulation of the intact elements near the crack tip as shown in Fig. 1.10.

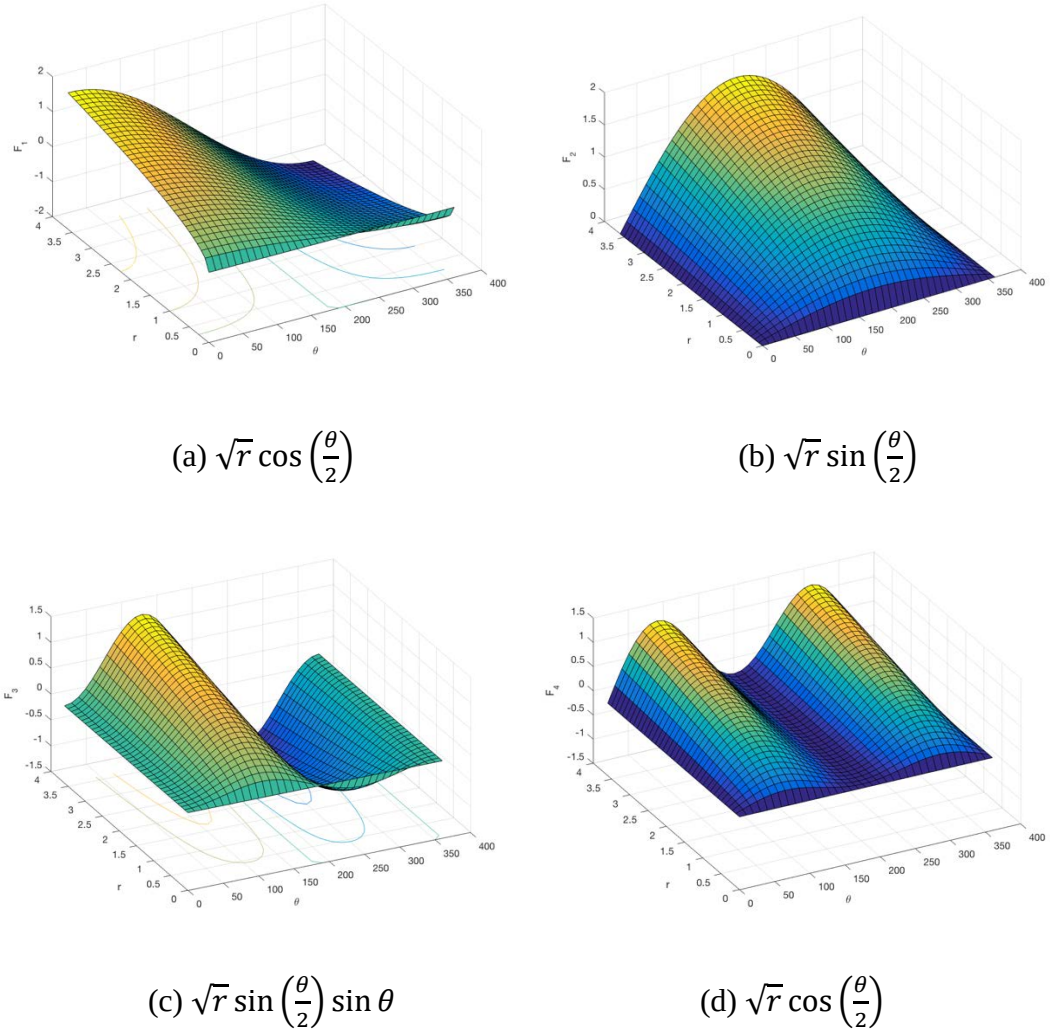

(a) $\sqrt{r}\cos\left(\frac{\theta}{2}\right)$ (b) $\sqrt{r}\sin\left(\frac{\theta}{2}\right)$

(c) $\sqrt{r}\sin\left(\frac{\theta}{2}\right)\sin\theta$ (d) $\sqrt{r}\cos\left(\frac{\theta}{2}\right)$

Figure 1.10. Enrichment functions around a crack tip

Heaviside function

For the enrich elements that are cut completely by a crack, we adapt a jump function, Heaviside function. It provides a method of Mathematics to model the behavior of the jump discontinuity in the displacement field when the splitting of the domain happens as a crack.

Denoted Γ with the crack within the domain Ω which is represented by a continuous curve, x (x, y) with the coordinate of the point in the domain, and x′ (x', y') with the coordinate of the closest point on the crack curve, and $\vec{\mathrm{n}}$ with the outward normal vector of curve Γ at point x′, the Heaviside function is defined as

$$H(x,y) = \begin{cases} 1 & \text{if} \quad (\mathrm{x} - \mathrm{x}') \cdot \vec{\mathrm{n}} > 0 \\ -1 & \text{if} \quad (\mathrm{x} - \mathrm{x}') \cdot \vec{\mathrm{n}} < 0 \end{cases} \tag{1.41}$$

H(x) will be positive if the vector $(\mathrm{x} - \mathrm{x}')$ is on the con side of the $\vec{\mathrm{n}}$ and negative on the pro side of the $\vec{\mathrm{n}}$.

Now we are ready to derive the complete enrichment approximation around a crack tip. Consider a finite element model of a domain with a crack shown in Fig. 1.11. D represents all the nodes in the domain, S_C denotes the set of nodes of elements around the crack tip, and S_H is the set of nodes of element along the crack.

Introducing the Heaviside function into Eq. 1.38, and substituting the basic enrichment function Eq. 1.40 into Eq. 1.38, the complete approximation in XFEM is presented as

$$u^h(\mathrm{x}) = u^h(\mathrm{x})_{FEM} + u^h(\mathrm{x})_{ENRD} \tag{1.42}$$

$$= \sum_{I=1}^{N} N_I(\mathrm{x})\, u_I + \sum_{I}^{N} \sum_{J \in S_H} N_J\big(H(\mathrm{x}) - H(\mathrm{x}_I)\big)\, t_J$$

$$+ \sum_{I=1}^{N} \sum_{J \in S_{C1}} \sum_{l=1}^{4} N'_J(\mathrm{x})[F_l^{C1}(\mathrm{x}) - F_l^{C1}(\mathrm{x}_I)]\, t_J$$

$$+ \sum_{I=1}^{N} \sum_{J \in S_{C2}} \sum_{l=1}^{4} N'_J(\mathrm{x})[F_l^{C2}(\mathrm{x}) - F_l^{C2}(\mathrm{x}_I)]\, t_J$$

where $F_l^{C1}(\mathrm{x})$ are defined as the enrichment functions around crack A and $F_l^{C2}(\mathrm{x})$ are defined around crack B, and S_{C1} and S_{C2} as the set of nodes of elements around Crack A and B, respectively.

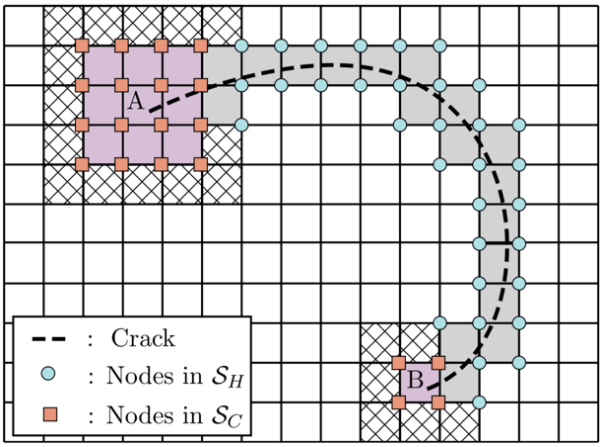

Figure 1.11. An enriched modeling of a crack with step enriched and tip enriched elements [36]

1.3.3 XFEM implementation in ABAQUS

ABAQUS provides the XFEM approach for modelling crack initiation and propagation.

In terms of the initiation, you can define the exact location for the crack. Alternatively, you can allow the system to determine where the crack initiates based on the fracture criterion you defined, for instance, the maximum principal stress or maximum or maximum principal strain calculated in the crack domain.

More importantly, ABAQUS is capable to determine the crack propagation in an arbitrary direction, that is, the system can identify in which direction the crack extends after the initiation. This is accomplished based on the XFEM and two methods are provided: cohesive segments method and LEFM segments method. For elastic material, LEFM approach is utilized and competent especially under loading of mixed mode. Generally, the two methods induce the similar result according to the manual of ABAQUS 2016 for brittle material. The theory utilized in the LEFM approach in ABAQUS is originated from Erdogan and Sih (1963), same as the fracture criterion introduced in Chapter 1, the direction of the crack propagation is given by

$$\hat{\theta} = cos^{-1}\left(\frac{3{K_{\mathrm{II}}}^2 + \sqrt{{K_{\mathrm{I}}}^4 + 8{K_{\mathrm{I}}}^2 K_{\mathrm{II}}^2}}{K_{\mathrm{I}}^2 + 9K_{\mathrm{II}}^2}\right) \tag{1.43}$$

where $\hat{\theta}$ is denoted with crack propagation angle and is measured with respect to the crack plane. Under pure Mode II loading, the equation above gives the angle of propagation as $70.5°$ while XFEM based LEFM approach in ABAQUS predicts the angle as $66.5°$.

2.0 UNIAXIAL COMPRESSION TEST ON PRISMATIC BRITTLE SAMPLES WITH EXCAVATION OF DIFFERENT GEOMETRIES

Tunnels are widely utilized in underground constructions. Different shapes of the excavations are presumed to influence the distribution and magnitude of stress on the boundaries. Finite element analysis is utilized to simulate the compression test and direct shear test on brittle prismatic samples with openings of different geometries. Those openings with smaller degree of curvature are expected to develop greater stresses at their boundaries. Consistently, those with higher degree of curvatures at their boundaries are expected to develop less boundary stresses. In the following sections, a finite element analysis will be used to show that whether the above statements are correct.

2.1 FINITE ELEMENT METHOD

Finite element method (FEM) was initially utilized in the 1960s and has been applied widely to the engineering realm since then. Much work has been done to combine the finite element method with rock mechanics [38]. Material heterogeneity, linear and non-linear deformability, complex boundary conditions, in situ stresses and gravity can all be derived by using this method.

2.1.1 Test formulation

Five types of tunnels with different geometries of excavations are simulated in ABAQUS as shown in Fig. 2.1. The material characteristics are shown in Table 2.1. The Poisson ratio is taken as 0.3. Considering the water content is around 3% at test, the young's modulus of the clay is determined to be 0.56 MPa (see Fig. 2.2). The Poisson ratio is taken to be 0.3.

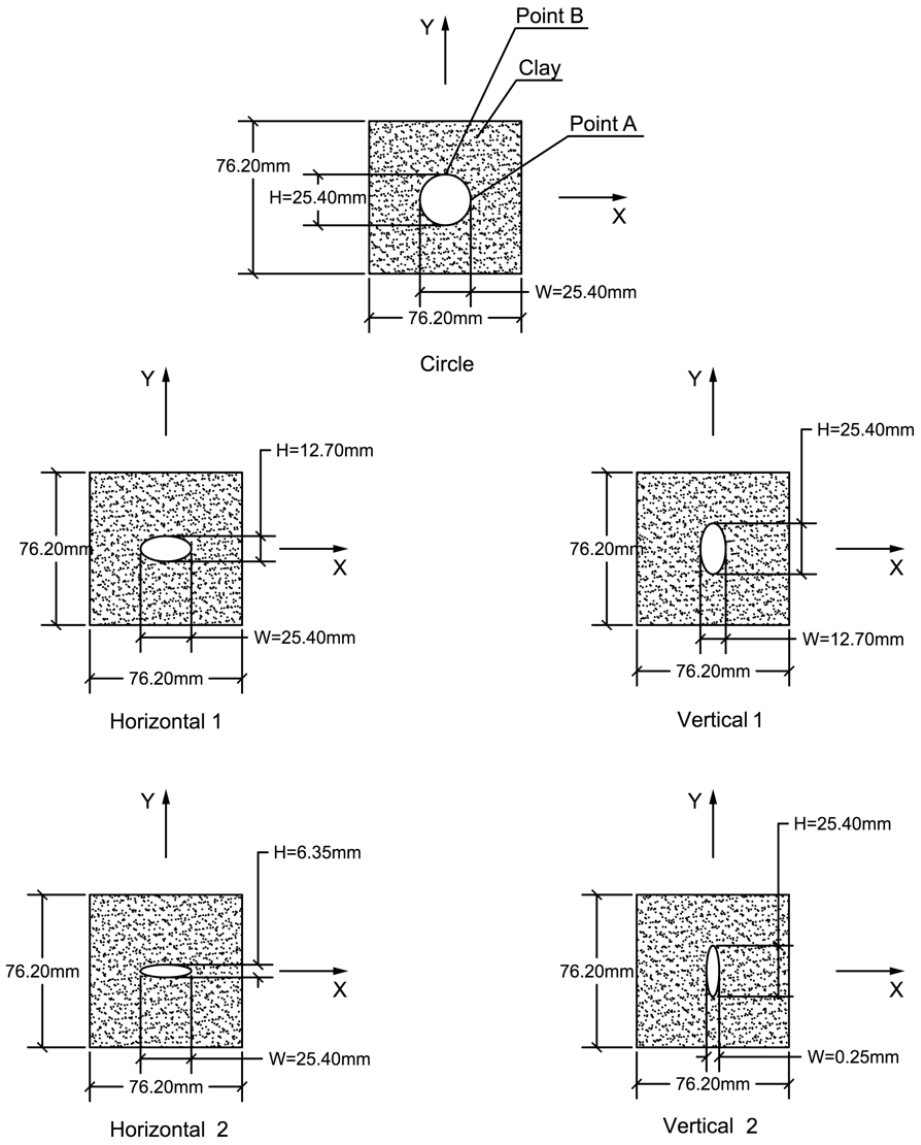

Figure 2.1. Five different geometries

Table 2.1. Material properties of stiff clay in simulations

Young's Modulus, MPa	0.56
Poisson's ratio	0.30
Density, kN/m^3	2.00

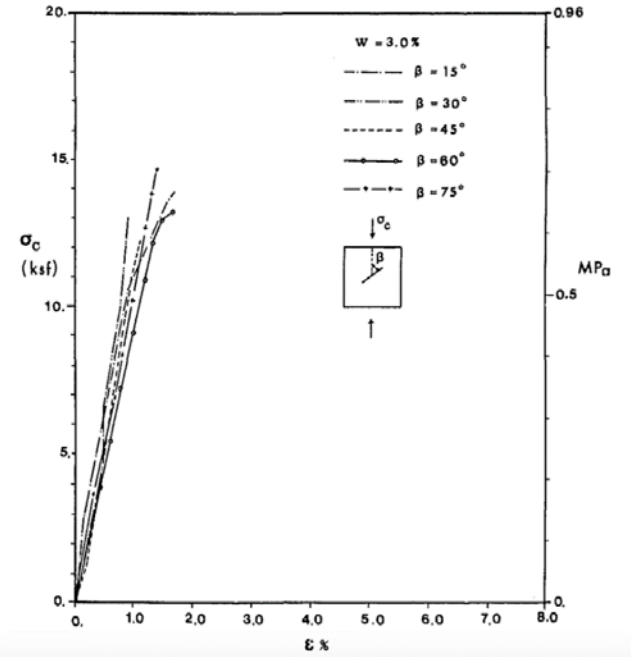

Figure 2.2. Stress – strain relationships of stiff clay at water content of 3% [40]

An explicit finite element method is utilized in the simulation, and the step time is set as 1 sec.

A pair of load and boundary is tested with the implicit method; however, the boundary cannot respond with the force in equilibrium. Instead, velocity of 0.1mm/s [41] is added on the top and the bottom sides, as shown in Fig. 2.3.

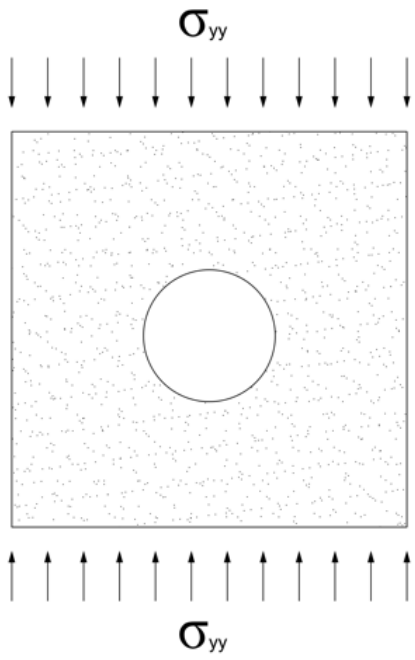

Figure 2.3. Boundary conditions and load conditions for uniaxial compression test

Considering the real test is conducted on the plane stress direct shear apparatus (PSDSA), the plane stress element is selected, CPS4R, a 3-node bilinear plane stress quadrilateral, reduced integration, hourglass control element is selected as the element for this study. There is one integration point in the center of the element. The mesh contribution is shown in Fig. 5. As seen in the figure, concentration is located at the significant area around the excavation. This is accomplished with the tool of partition, with which the area is divided into two parts, the inner circular area around the excavation and the remainder of the sample. The mesh size is 0.3mm in the inner boundary, 0.6 mm on the partition circle and 2.5mm on the external boundary. This method reduces the number of elements and is calculation economized. The determination of the mesh size is based on the convergence test until the difference between the two trial size is less than 2%.

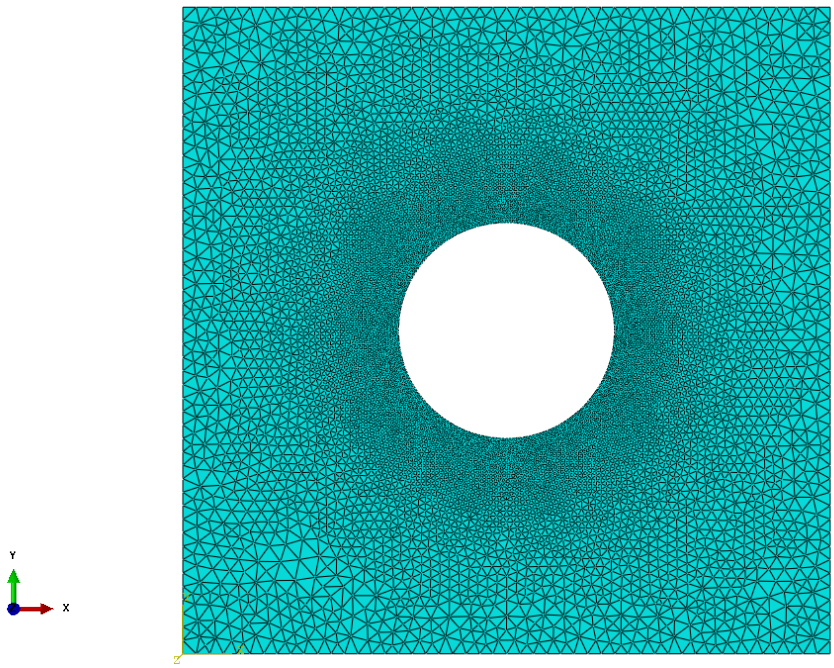

Figure 2.4. Mesh strategy in ABAQUS

2.1.2 Result analysis

The stress contour of each case is shown in Fig. 2.5- 2.9.

Stress in the x direction and y direction is noted in order to obtain both the maximum tension at point B, which is in x direction and the maximum compression at point A, which is in y direction. The location of point A and point B is indicated in Fig. 2.1.

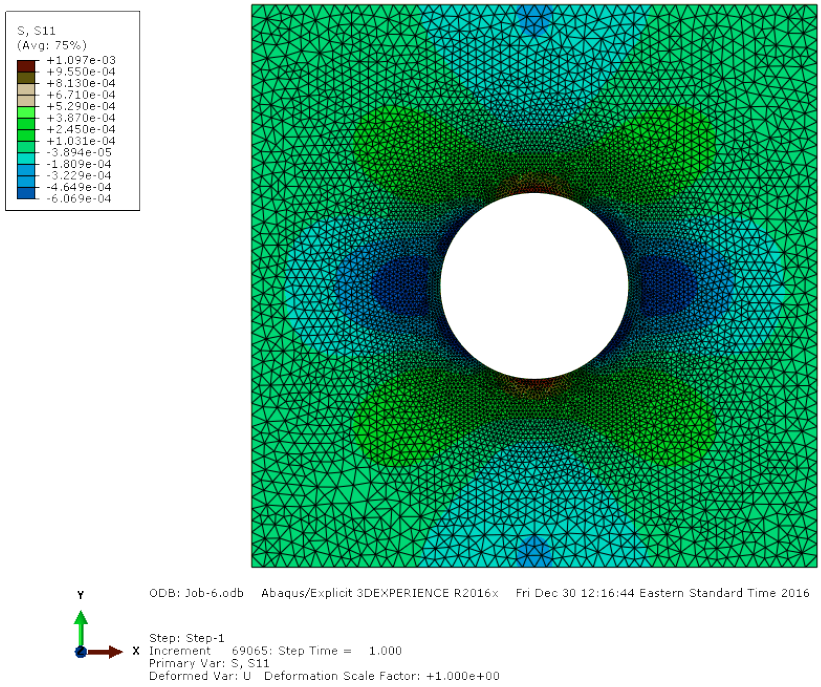

(a)

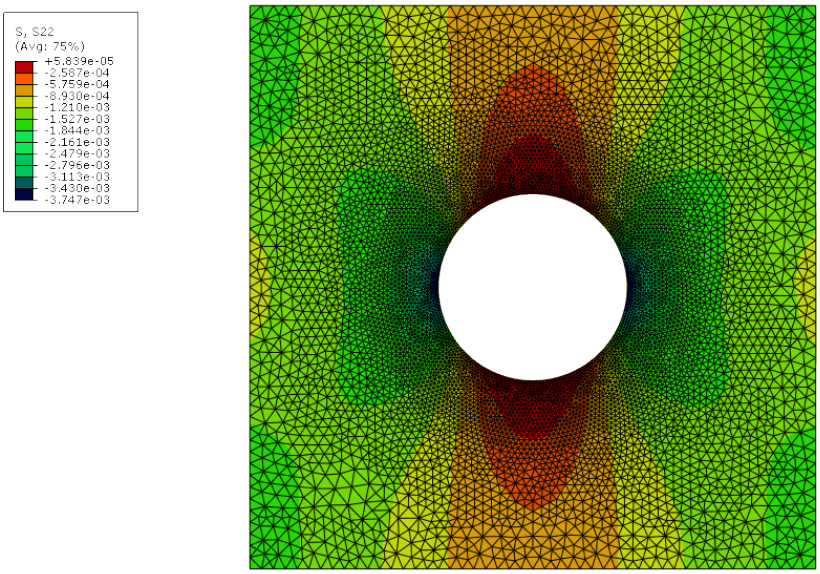

(b)

Figure 2.5. Stress contour for circular excavation: (a) stress in x direction, s11; (b) stress in y direction, s22

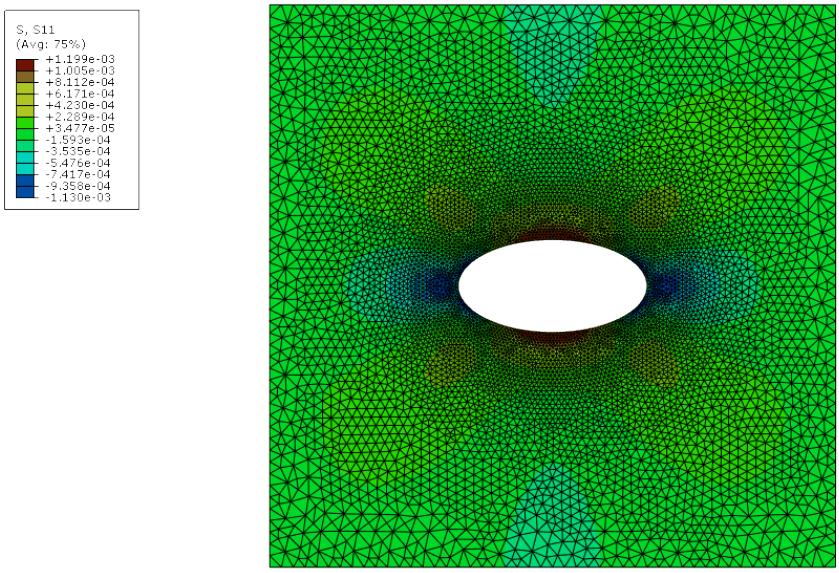

(a)

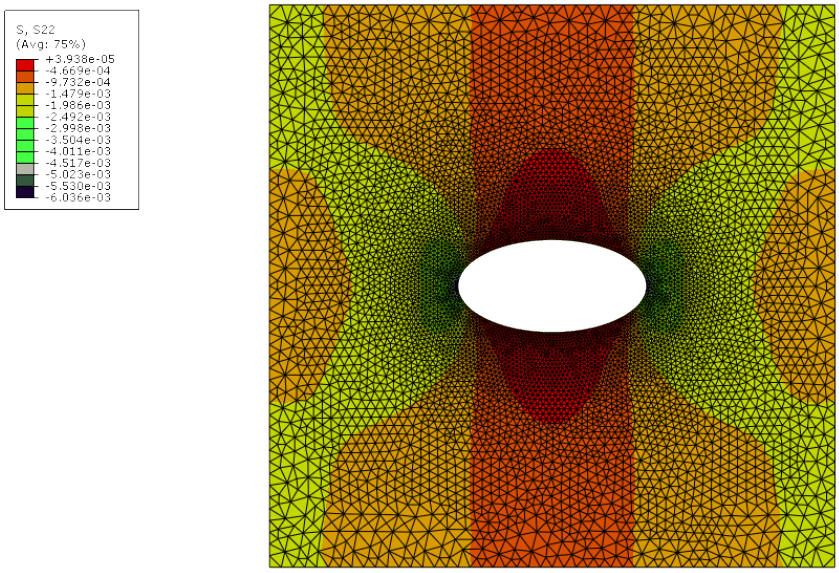

(b)

Figure 2.6. Stress contour for horizontal elliptical excavation 1: (a) stress in x direction, s11; (b) stress in y direction, s22

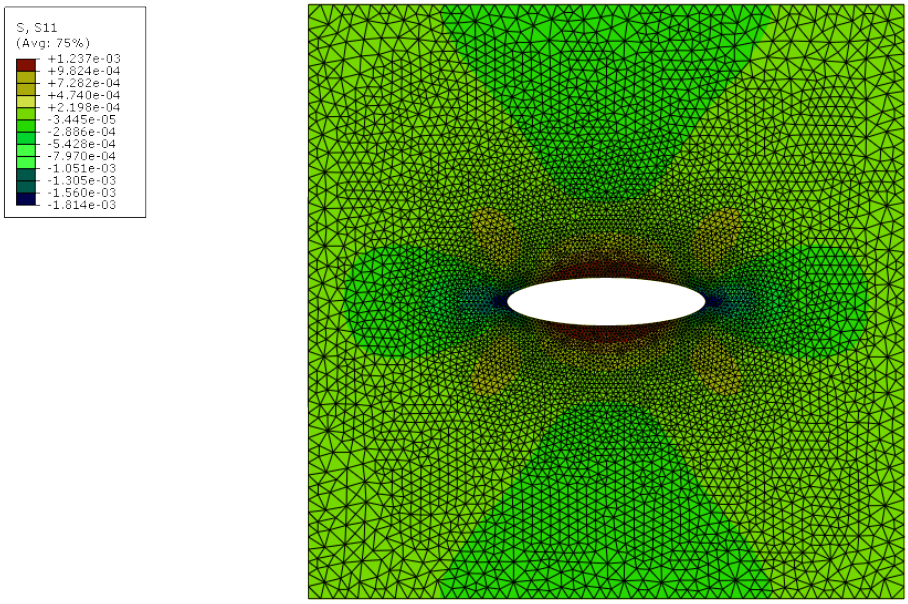

(a)

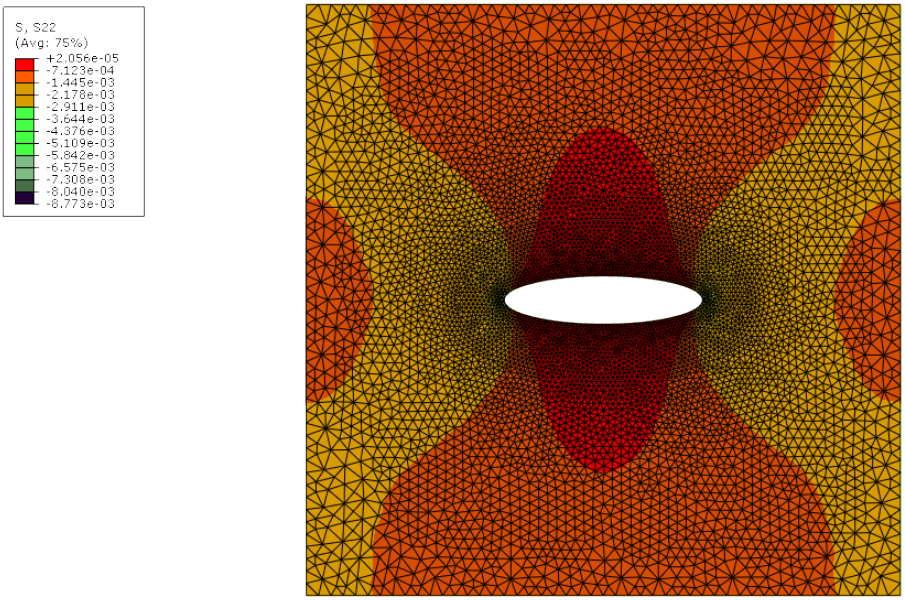

(b)

Figure 2.7. Stress contour for horizontal elliptical excavation 2: (a) stress in x direction, s11; (b) stress in y direction, s22

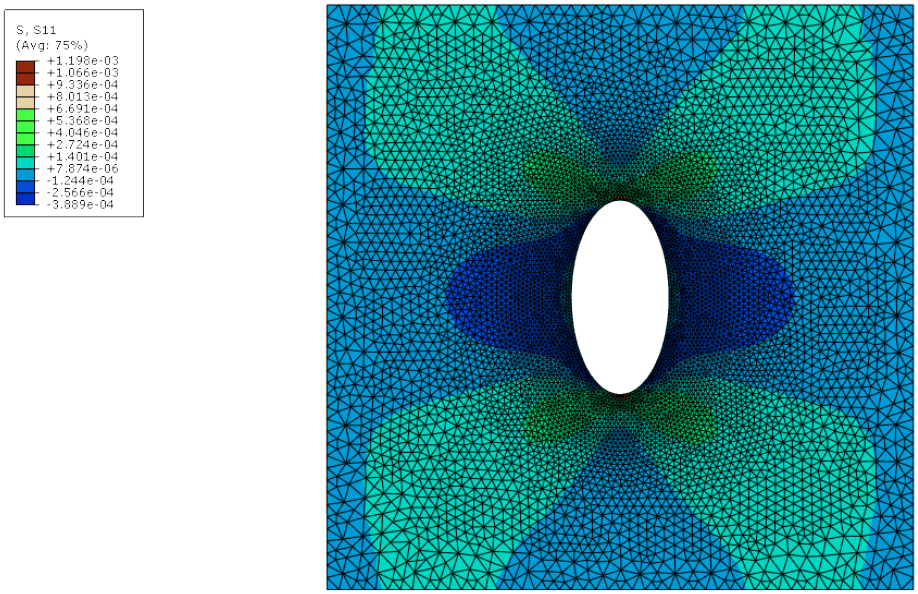

(a)

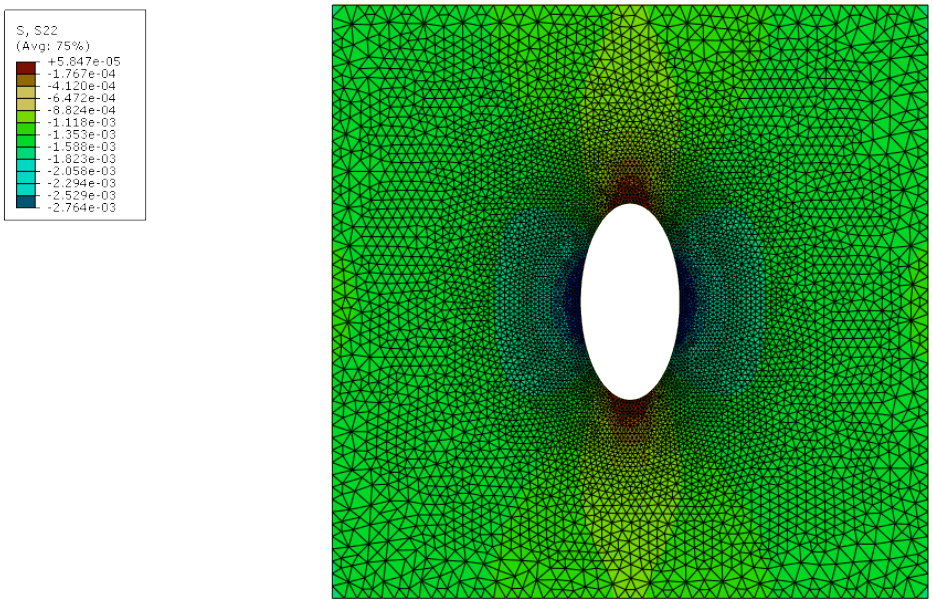

(b)

Figure 2.8. Stress contour for vertical elliptical excavation 1: (a) stress in x direction, s11; (b) stress in y direction, s22

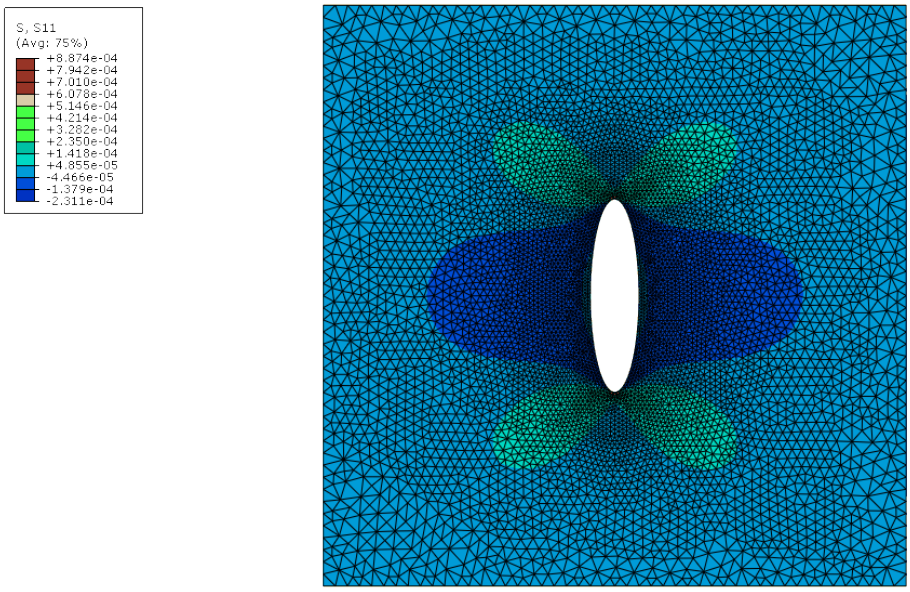

(a)

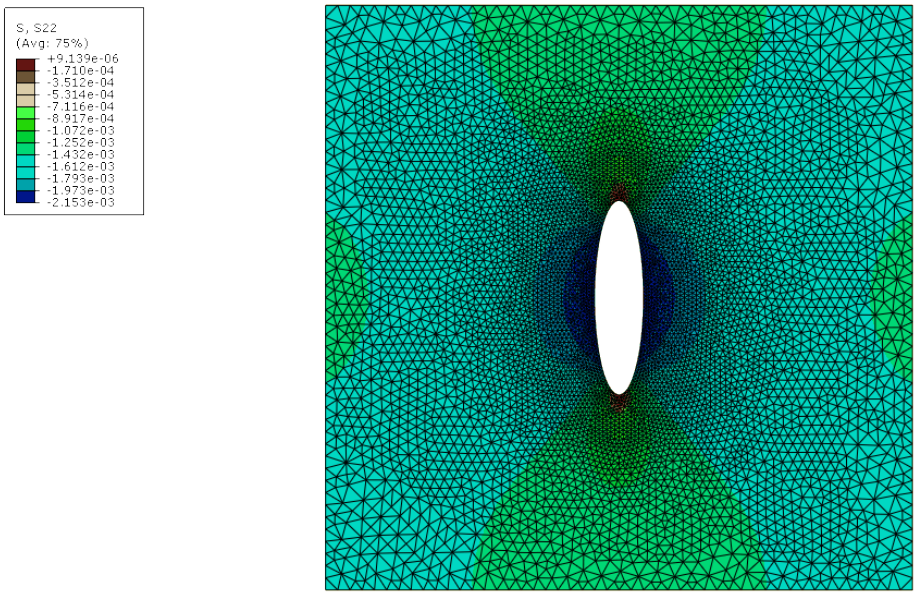

(b)

Figure 2.9. Stress contour for vertical elliptical excavation 2: (a) stress in x direction, s11; (b) stress in y direction, s22

As shown in the contour, maximum tension in x direction, $\sigma_{xx,max}$, is induced at point B. Maximum compression in y direction, $\sigma_{yy,max}$, is induced at point A as shown in the stress contours. These results are consistent with what is expected. The maximum critical stresses of each case are shown in Table 2.2.

Table 2.2. Maximum critical stresses of each case

	Vertical 2	Vertical 1	Circle	Horizontal 1	Horizontal 2
W/H	0.25	0.5	1	2	4
$\sigma_{xx,max}$ at point B	0.88E-03	1.20E-03	1.10E-03	1.20E-03	0.80E-3
H/W	4	2	1	0.5	0.25
$\sigma_{yy,max}$ at point A	2.15E-03	2.76E-03	3.75E-03	5.99E-03	8.77E-03

The magnitude of openings at point B can be depicted by the values of W/H, and magnitude of openings at point A can be depicted by the values of H/W, where $H = Height\ of\ Excavation, W = Width\ of\ Excavation$. In addition, the variations of maximum stresses when the degree of openings increases are shown in Fig. 2.10. (a) and (b). It is indicated that the maximum compression $\sigma_{yy,max}$ at point A decreases as the degree of opening at the concentration grows - that is to say, the excavation with the larger opening at the compression concentration presents lower $\sigma_{yy,max}$ than that with narrow opening. However, the theory doesn't apply to the analysis of tension. The maximum tension $\sigma_{xx,max}$, which is located at point B exhibits the fluctuating magnitude as the degree of opening increases. The results present the conversed law with respect to the expected principal, that is, the minimum value happens at the acutest

opening. In another word, the elliptical excavation with the most acute crown exhibits the lowest tension. In conclusion, the influence of the degree of the opening on the magnitude of compression is reasonable and consistent with the expected principle - that is, the concentration with a larger opening (the positive direction of x axis in both two plots) produces lower compression. Conversely, the concentration with a smaller opening produces lower tension.

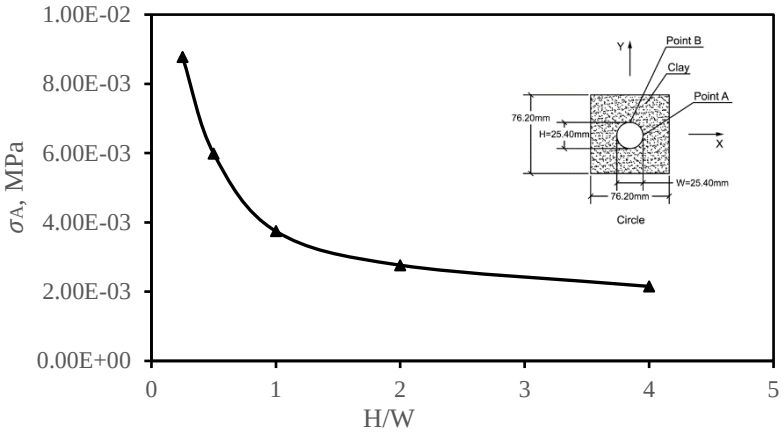

(a)

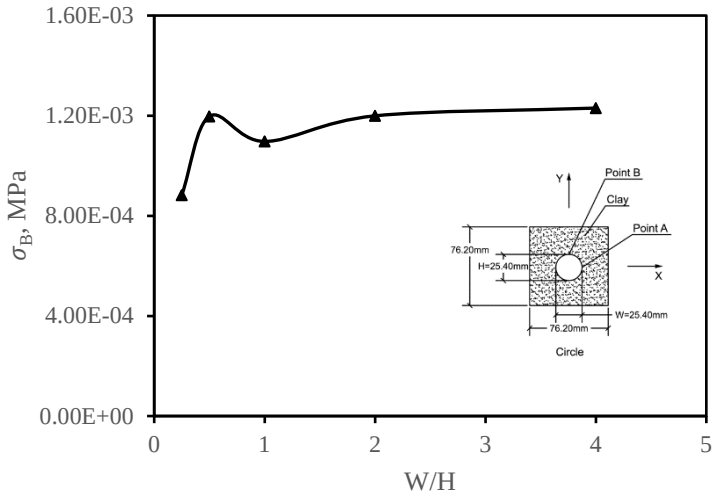

(b)

Figure 2.10. Variations of (a) $\sigma_{yy,max}$ at point A and (b) $\sigma_{xx,max}$ at point B

2.2 LINEAR ELASTIC FRACTURE MECHANICS

2.2.1 Circular excavation

The tangential stress around the opening is obtained through LEFM by Kirsch [11] as

$$\sigma_{\theta\theta} = \frac{P}{2}\left[(1+K)\left(1+\frac{a^2}{r^2}\right)+(1-K)\left(1+\frac{3a^4}{r^4}\right)cos2\theta\right] \tag{2.1}$$

In this case,

$$\begin{gathered} \mathrm{K} = 0 \\ \mathrm{a} = \mathrm{r} \\ \theta = 90° \text{ for point B} \\ \theta = 0° \text{ for point A} \end{gathered} \tag{2.2}$$

Substituting these conditions into the equation above, we have

At point A:

$$\sigma_B = 3P = 3 \times 0.001148 = 0.003444 \text{ MPa}, compression \tag{2.3}$$

At point B:

$$\sigma_A = -P = -0.001148 \text{ MPa}, Tension \tag{2.4}$$

Comparison between the stresses from FEM and that from LEFM is shown in Table 2.3.

Table 2.3. Stress results from FEM and LEFM for circle

	FEM Method, a	LEFM Method, b	Differences, (a-b)/b
σ_A, MPa	3.75E-03	3.44E-03	9.01%
σ_B, MPa	1.10E-03	1.14E-03	3.51%

2.2.2 Elliptical excavation

The cross section for the Ellipse excavation is shown in Fig. 2.11. σ_B and σ_A are derived by B. H. G. Brady & E. T. Brown. as

$$\sigma_A = p(1 - K + 2q) \tag{2.5}$$

$$\sigma_B = p\left(K - 1 + \frac{2K}{q}\right) \tag{2.6}$$

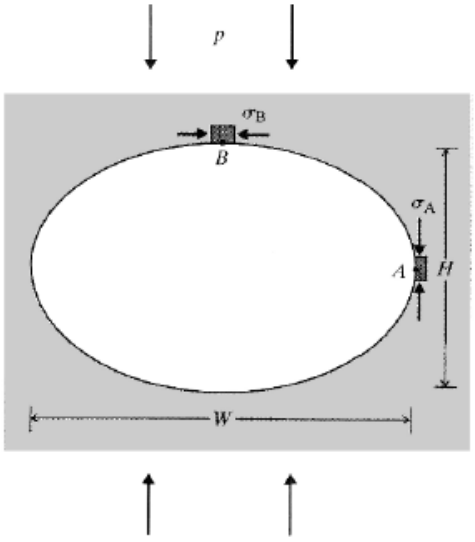

Figure 2.11. Geometry for the elliptical excavations specifying the stresses at point A and B under uniaxial stress field [13]

In this case, $K = 0$. Hence, the equations are reduced to

$$\sigma_A = p(1 + 2q)$$
$$\sigma_B = -p \tag{2.7}$$

where

$$
\begin{aligned}
p = 0.001193\ MPa, q = \frac{W}{H} = 2\ for\ H1 \\
p = 0.001219\ MPa, q = \frac{W}{H} = 4\ for\ H2 \\
p = 0.001351\ MPa, q = \frac{W}{H} = 0.5\ for\ V1 \\
p = 0.001424\ MPa, q = \frac{W}{H} = 0.25\ for\ V2
\end{aligned}
\tag{2.8}
$$

The theoretical results, compared with the FEM results, are shown in Table 2.4

Table 2.4. Stress results from FEM and LEFM for ellipse

		FEM Method	LEFM Method
H1	σ_A , MPa	5.99E-03	5.97E-03
	σ_B, MPa	1.20E-03	1.19E-03
H2	σ_A , MPa	8.77E-03	10.97E-03
	σ_B, MPa	0.80E-03	1.22E-03
V1	σ_A , MPa	2.76E-03	2.70E-03
	σ_B, MPa	1.20E-03	1.35E-03
V2	σ_A , MPa	2.15E-03	2.14E-03
	σ_B, MPa	0.88E-03	1.42E-03

2.3 COMPARISON BETWEEN XFEM AND LEFM APPROACH

The results from numerical analysis and theoretical analysis of the maximum tension and compression are shown in Fig. 2.12. (a) and (b) respectively. These results indicate that these two methods produce more precise results at the concentrations with larger opening. With the openings with smaller magnitudes, the results from FEM are much lower than that from LEFM for both tension and compression. Furthermore, the difference between the two methods becomes increasingly larger when the opening of the concentration becomes smaller. Generally, the

compression or tension modeled by FEM is closer to the theoretical solution when the opening at the concentration point is larger. Both results show that at point A, the compression decreases as the magnitude of openings grows, whereas, at point B, the magnitude of tension does not vary that much.

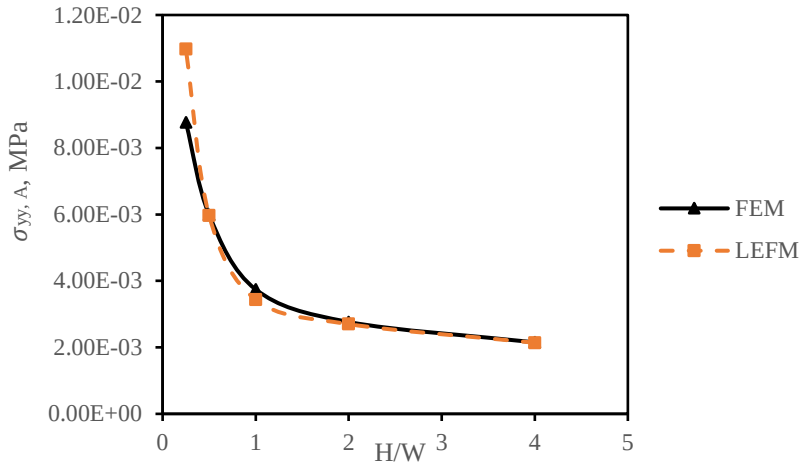

(a)

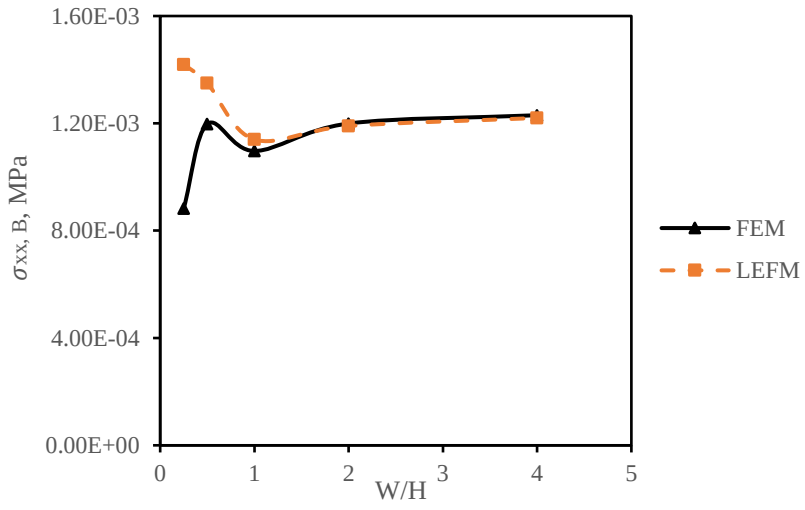

(b)

Figure 2.12. Comparisons between Numerical Analysis Using FEM and Theoretical Analysis Using LEFM on the stress at (a) Point A; and (b) Point B

3.0 DIRECT SHEAR TEST ON PRISMATICS BRITTLE SAMPLES WITH OPENINGS OF DIFFERENT SHAPES

3.1 FINITE ELEMENT METHOD

3.1.1 Test formulation

The geometry, mesh strategy, and material properties in the simulation of the direct shear test are same as those in uniaxial test. The system of stresses acting on the soil element located in the shear zone during direct shear test are shown in Fig. 3.1. Based on this framework, the loading system applied in the direct shear test is transformed to the equivalent stress field on the soil element, as shown in Fig. 3.2. Normal stresses applied on four external boundaries are taken as 7.81e-4 MPa, and the shear stresses are taken as $3.35 \times 10^{-4}\ MPa$.

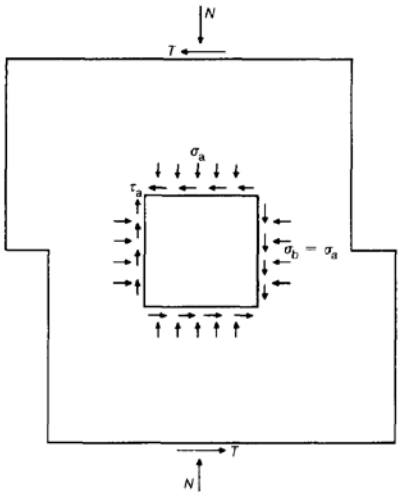

Figure 3.1. Stresses acting on a soil element on the failure surface in the direct shear test

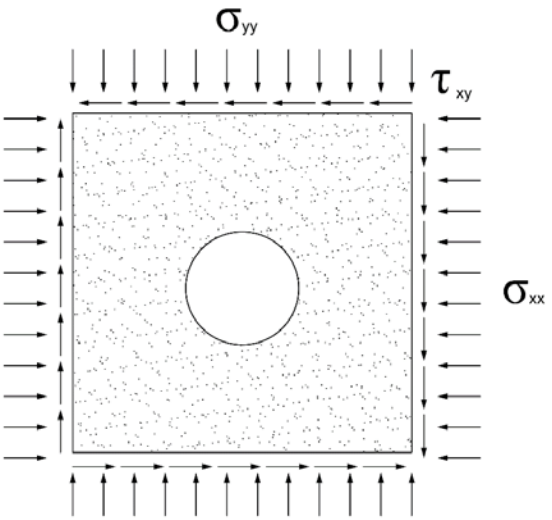

Figure 3.2. Load condition in the direct shear test utilizing the equivalent stress field of a soil element on the failure surface

3.1.2 Result analysis

The stress contour of each geometry is shown in Fig. 3.3 to 3.7.

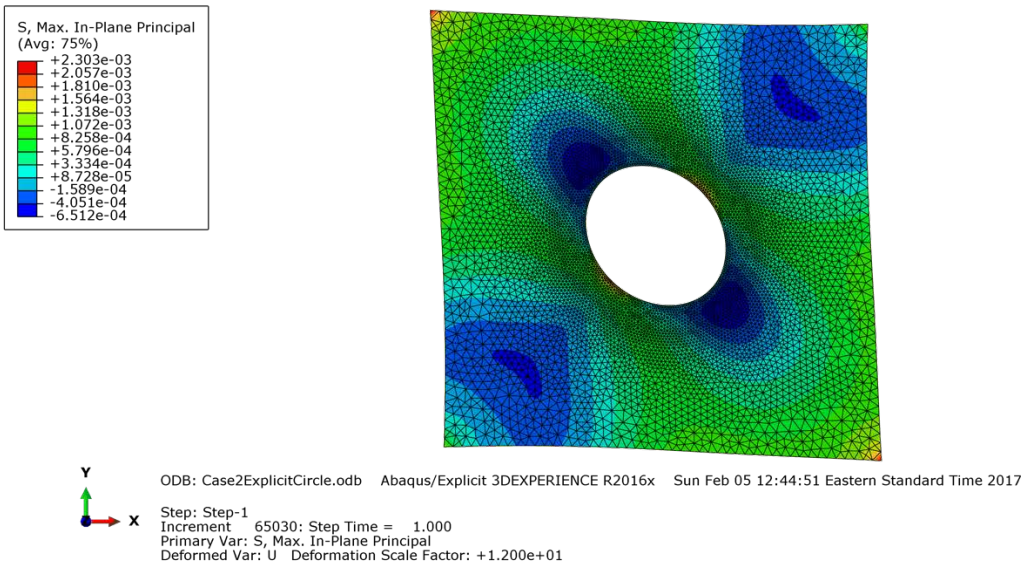

(a)

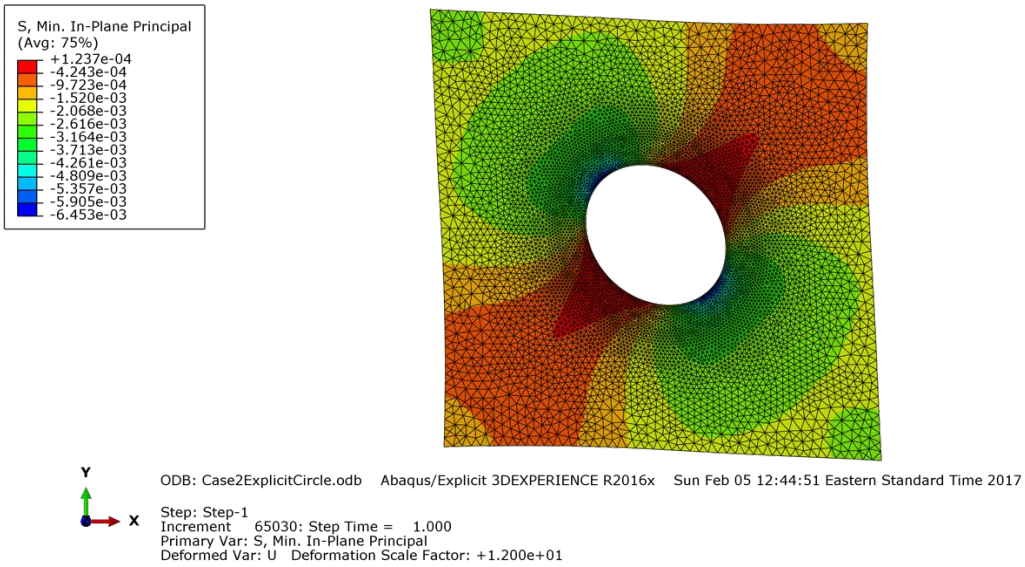

(b)

Figure 3.3. Stress contour for circular excavation: (a) maximum principal stress; (b) minimum principal stress

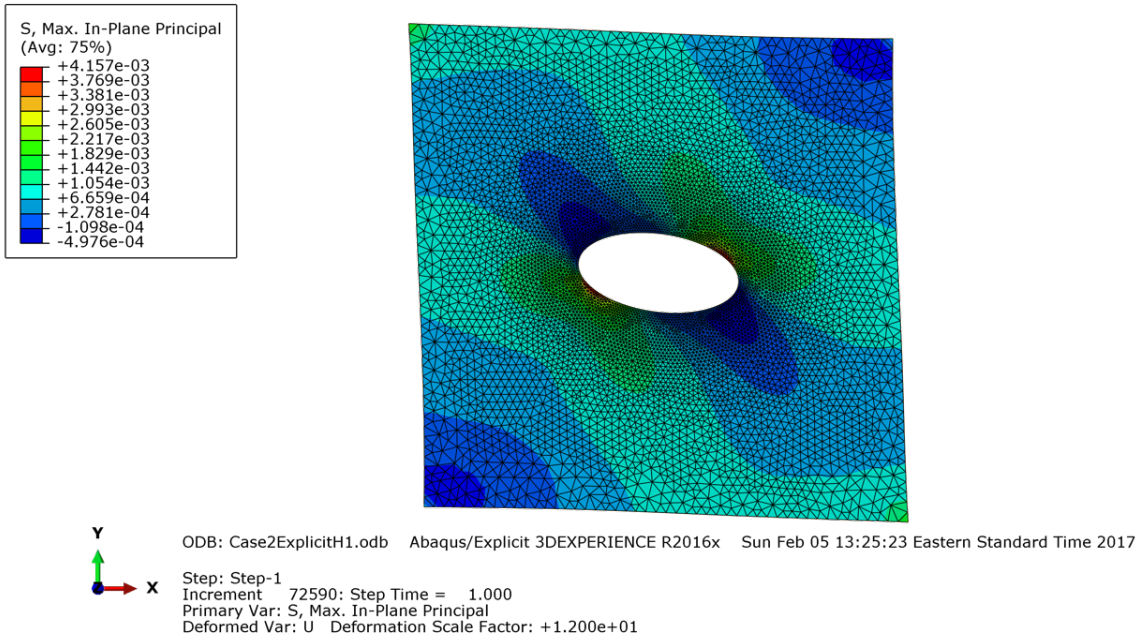

(a)

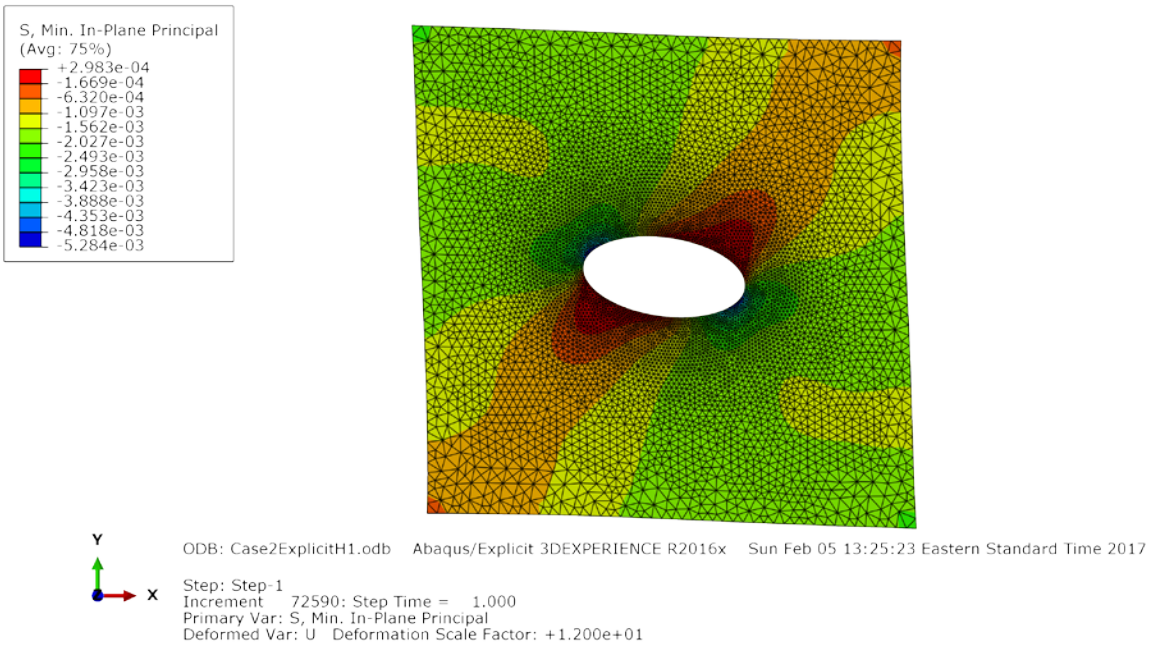

(b)

Figure 3.4. Stress contour for horizontal elliptical excavation 1: (a) maximum principal stress; (b) minimum principal stress

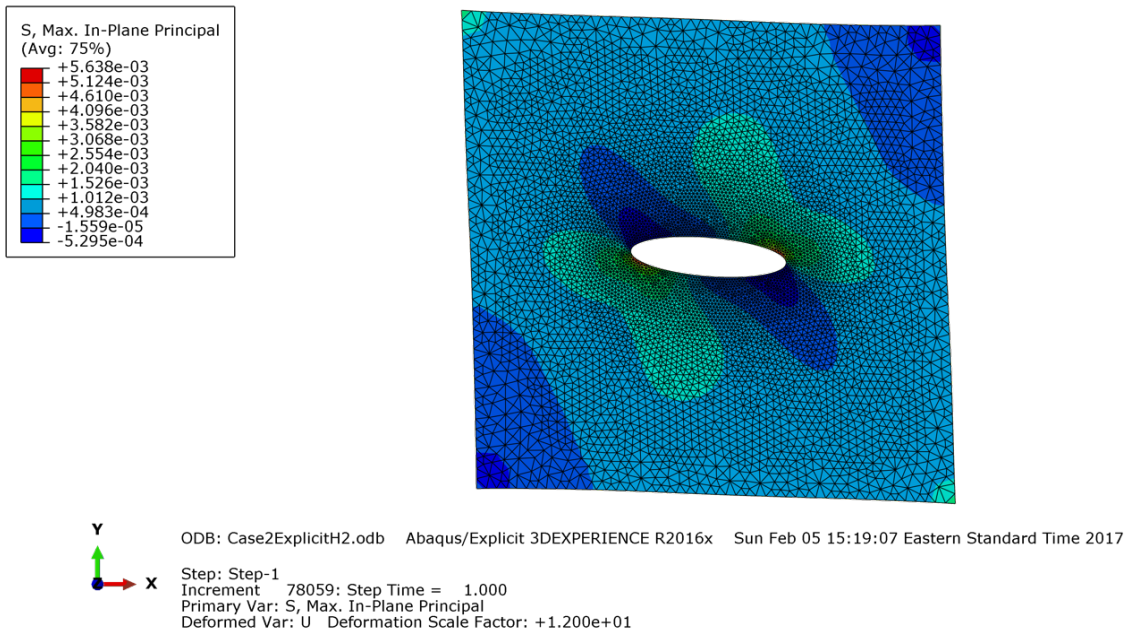

(a)

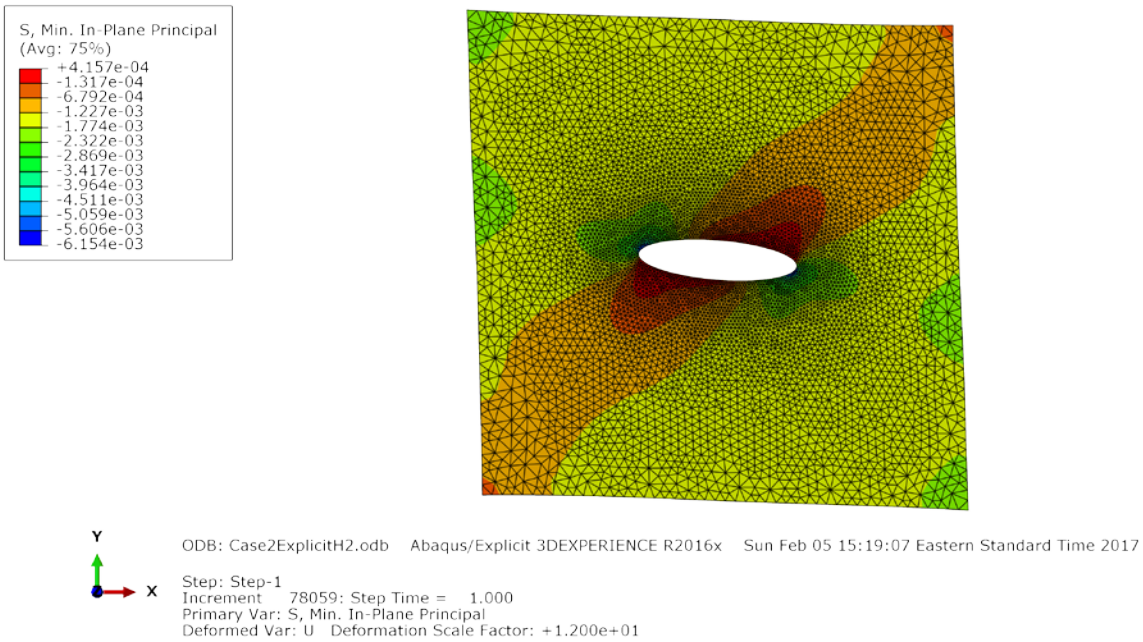

(b)

Figure 3.5. Stress contour for horizontal elliptical excavation 2: (a) maximum principal stress; (b) minimum principal stress

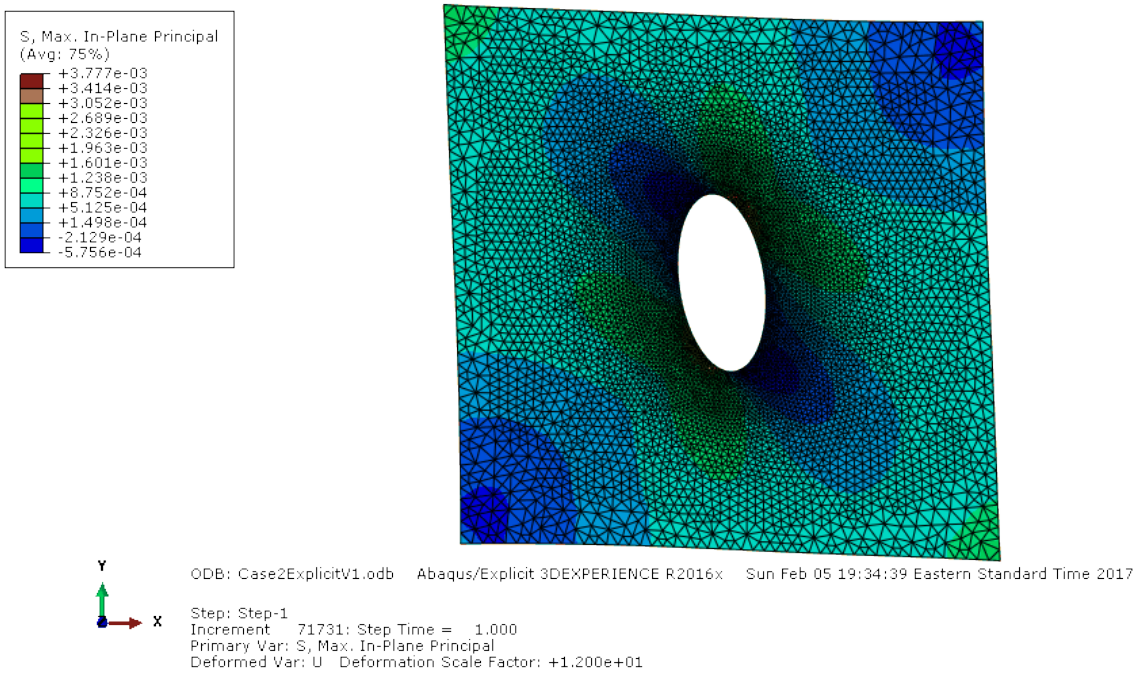

(a)

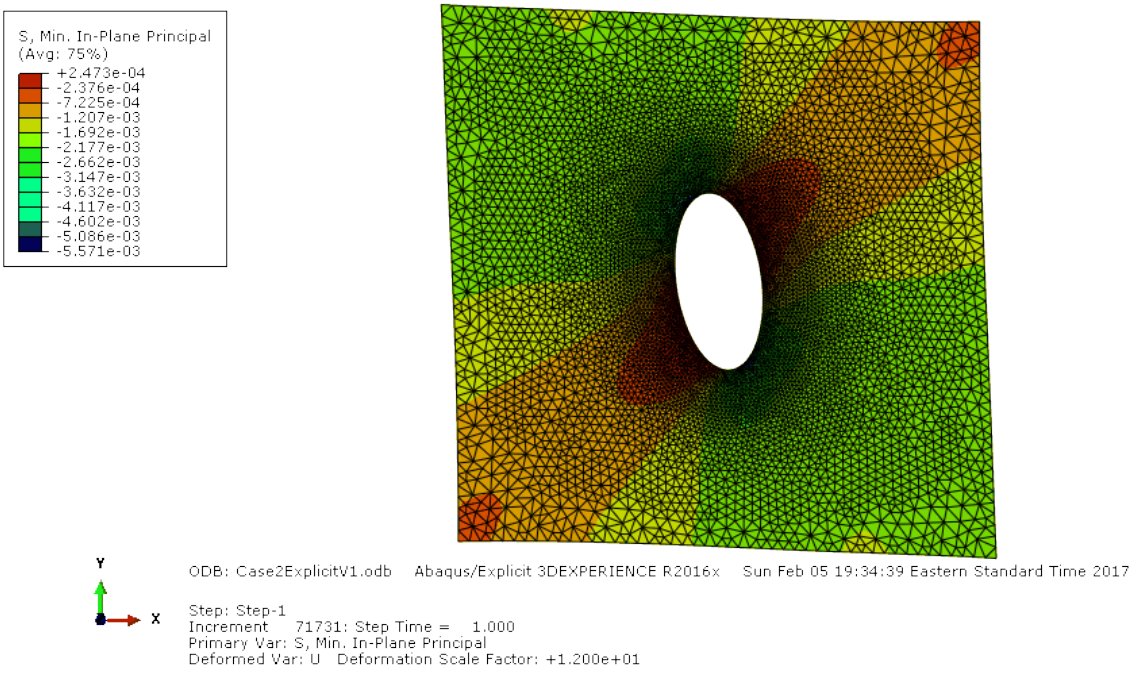

(b)

Figure 3.6. Stress contour for vertical elliptical excavation 1: (a) maximum principal stress; (b) minimum principal stress

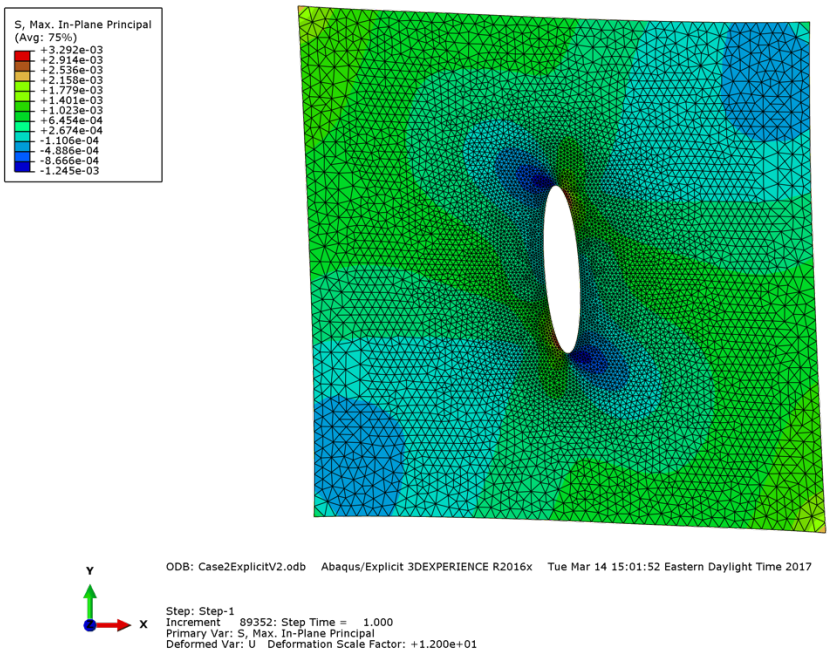

(a)

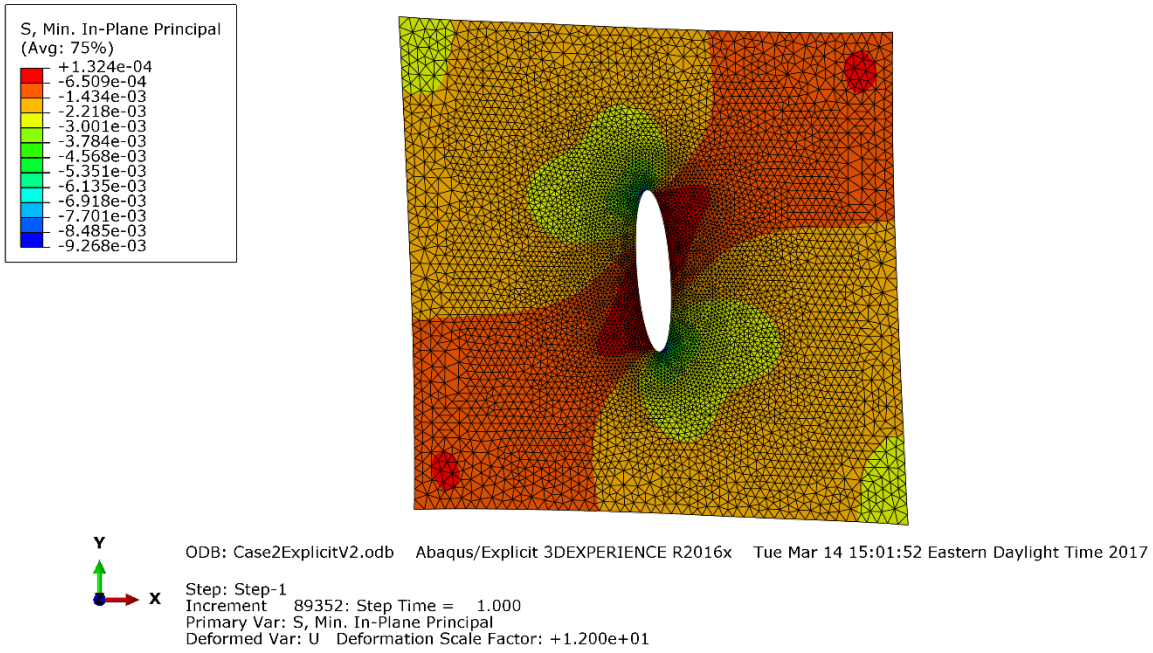

(b)

Figure 3.7. Stress contour for vertical elliptical excavation 2: (a) maximum principal stress; (b) minimum principal stress

It is worth noting that the compression and tension in ABAQUS is defined as negative and positive, respectively. Also, according to the boundary stress equation in LEFM, only tangential stress exists around the excavation. Hence, the maximum principal stress as well as the maximum tangential stress is associated with the maximum tension around the boundary excavation, and the minimum principal stress as well as the minimum tangential stress is associated with the maximum compression. This illustrates why the maximum principal stress and the minimum principal stress are exported in this case. As shown in the contour, the maximum compression and tension are no longer induced at point A nor point B. The maximum tension σ_t and compression σ_c are shown in Table 3.1.

Table 3.1. Maximum critical stresses with FEM method in direct shear test

	Vertical 2	Vertical 1	circle	Horizontal 1	Horizontal 2
W/H	0.25	0.5	1	2	4
$\sigma_{t,max}$, MPa	5.02E-04	2.16E-04	1.25E-04	2.15E-04	4.82E-04
H/W	4	2	1	0.5	0.25
$\sigma_{c,max}$, MPa	7.50E-03	4.61E-03	3.69E-03	4.56E-03	7.56E-03

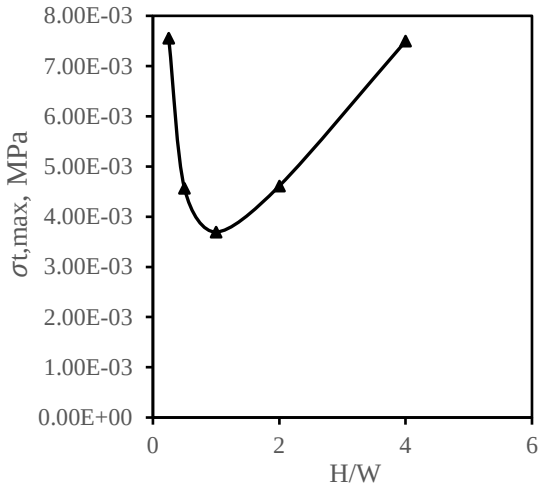

(a)

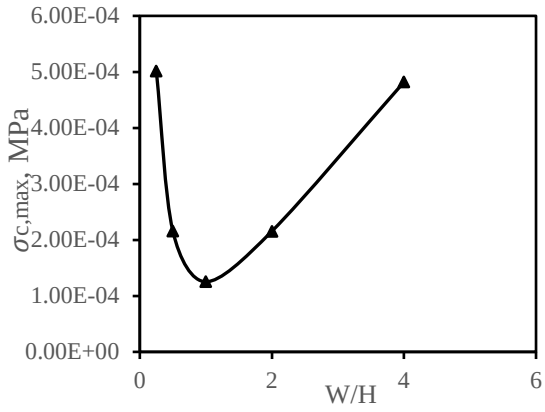

(b)

Figure 3.8. Variation of (a) $\sigma_{t,max}$ and (b) $\sigma_{c,max}$ when degree of opening at the corresponding concentration increases

Furthermore, variations in maximum tension and compression that are found as the degree of opening increases are plotted in Fig. 3.8. (a) and (b). As shown in Fig. 3.8.a, $\sigma_{c,max}$ declined as the magnitudes of openings grows when H/W is smaller than one. In this case, the rule is consistent with that of the uniaxial test. After H/W exceeds one, the maximum stresses increase as the

magnitudes of openings grows. In other words, the geometry with H/W equals to 1 presents the lowest $\sigma_{c,max}$.

In Fig. 3.8. (b), it can be seen that before W/H reaches one, $\sigma_{t,max}$ decreases as the degree of the opening increases. After W/H exceeds one, $\sigma_{t,max}$ increases as the degree of opening increases. The geometry with W/H equals to one, i.e., the circular excavation exhibits the lowest $\sigma_{t,max}$ as well as the lowest $\sigma_{c,max}$ on the direct shear test.

3.2 LINEAR ELASTIC FRACTURE MECHANCIS

Given $\sigma_x = \sigma_y$, the angle, β between the transformed principle plane and the positive direction of $X - axis$ can be obtained by

$$\tan 2\beta = \frac{2\tau_{xy}}{\sigma_y - \sigma_x} \tag{3.1}$$

Hence,

$$\beta = 45°,$$

indicating that the principle plane is $45°$ counter-clockwise to the horizontal plane (see Fig. 3.9).

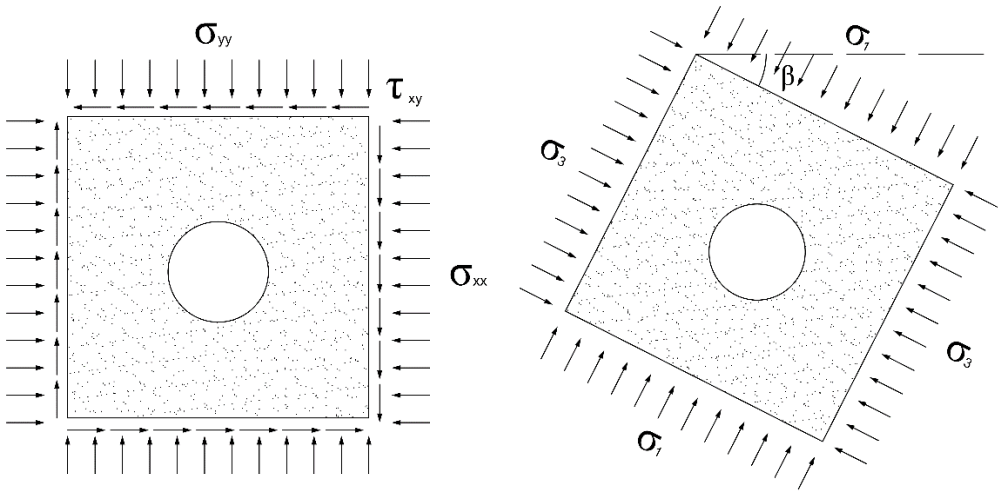

(a) (b)

Figure 3.9. Transformation of load conditions in direct shear test (a) original stress field; (b) transformed stress field

Next, the transformed stresses can be obtained using

$$\sigma_1 = \frac{\sigma_y + \sigma_x}{2} + \sqrt{\left(\frac{\sigma_y - \sigma_x}{2}\right)^2 + {\tau_{xy}}^2}$$
$$\sigma_3 = \frac{\sigma_y + \sigma_x}{2} - \sqrt{\left(\frac{\sigma_y - \sigma_x}{2}\right)^2 + {\tau_{xy}}^2} \quad (3.2)$$

The resulting principal stresses are shown in Table 3.2.

Table 3.2. Principal stresses transformed from the original stress field

σ_{xx}, MPa	σ_{yy}, MPa	τ_{xy}, MPa	σ_1, MPa	σ_3, MPa	$\beta, degree$
7.81E-04	7.81E-04	3.35E-04	1.12E-03	4.46E-04	4.50E+01

The tangential stress at any point of the excavation boundary can be obtained as

$$\sigma_t = \frac{2ab(\sigma_3 + \sigma_1) + (\sigma_3 - \sigma_1)[(a+b)^2 \cos 2(\beta - \eta) - (a^2 - b^2)\cos 2\beta]}{a^2 + b^2 - (a^2 - b^2)\cos 2\eta} \quad (3.3)$$

where a is the length of the elliptical axis on the x direction, b is the length of the elliptical axis on the y direction (a=b for circular excavation), β is the angle between σ_1 and x-axis, and η is defined as

$$\tan \eta = \frac{b}{a} \tan \theta \quad (3.4)$$

where θ is the angle of certain point with respect to positive x-axis. For different geometry, coordinates of concentration with maximum compression or tension stress are found based on the FEM results in order to find θ. The maximum critical compression and tension stresses can be calculated using Eq. 3.3, as shown in Table 3.3.

Table 3.3. Maximum compressions and tensions in FEM and LEFM for direct shear test

	Vertical 2	Vertical 1	circle	Horizontal 1	Horizontal 2
W/H	0.25	0.5	1	2	4
$\sigma_{t,max}$ LEFM, MPa	2.86E-04	-4.33E-05	-2.4E-04	-4.04E-05	2.81E-04
$\sigma_{t,max}$ FEM, MPa	5.02E-04	2.16E-04	1.25E-04	2.15E-04	4.82E-04
H/W	4	2	1	0.5	0.25
$\sigma_{c,max}$ LEFM, MPa	6.29E-03	3.86E-03	2.91e-03	3.82e-03	6.66e-03
$\sigma_{c,max}$ FEM, MPa	7.50E-03	4.61E-03	3.69E-03	4.56E-03	7.56E-03

3.3 COMPARISON BETWEEN XFEM AND LEFM APPROACH

In order to check the accuracy of FEM, comparison between FEM and LEFM is plotted in Fig. 3.10. As shown in the Figure, in simulating the compression, the result from FEM is close to the LEFM for different geometries. With regard to compression, the two methods have larger difference in the geometry for openings of smaller curvature. That is to say, when the curvature of the opening is smaller, the difference between the results of the two methods is greater. However, the two methods have a large difference in the results of tension stress. The magnitude of stress in LEFM results is lower than that in FEM results.

The difference is so greater since that the location in the FEM method for maximum tension is not accurate as the location in the LEFM approach. And the location from FEM is utilized to calculate the maximum tension in LEFM which accounts for the difference.

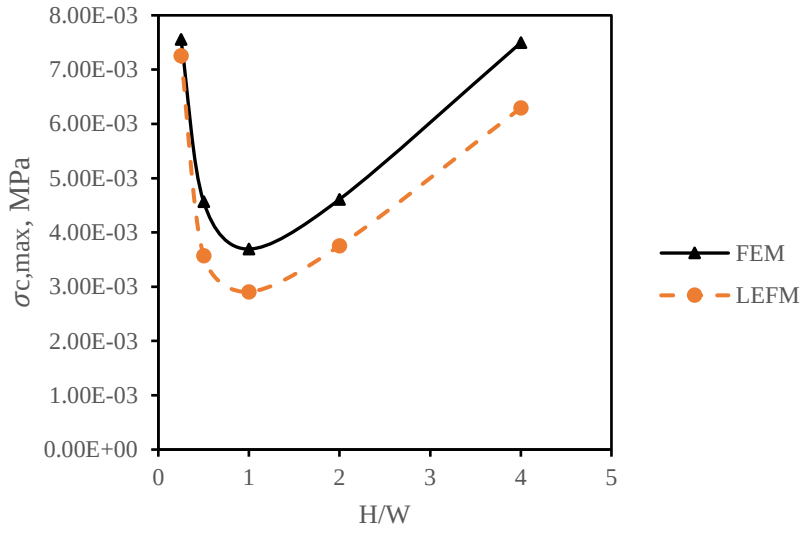

(a)

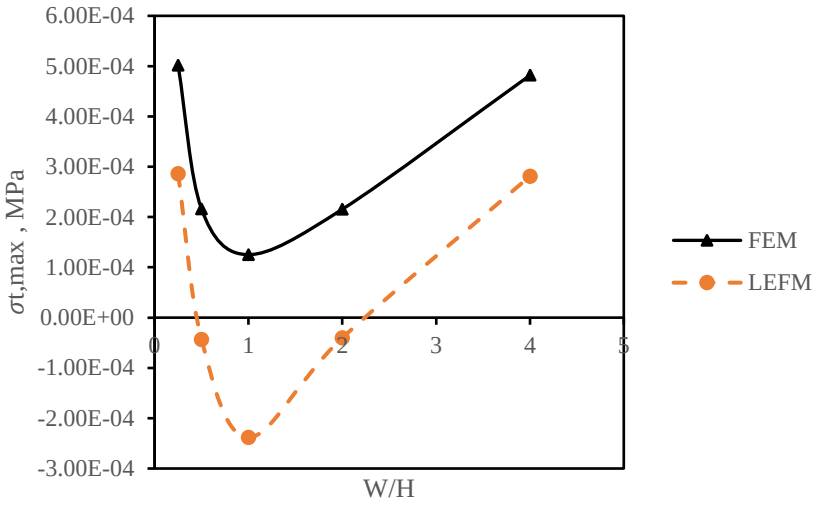

b)

Figure 3.10. Comparison between FEM and LEFM in conditions of maximum (a) compression and (b) tension stress with respect to the different degree of opening

4.0 DIRECT SHEAR TEST ON A SLOPE WITH A NOTCH AT ITS TOE

The influence of the fissures on the strength and failure characteristics of clay has been investigated by Vallejo [37]. Fracture criterion in LEFM theory has been applied to such problems and has been proved to be effective in predicting the crack propagation under mixed mode [39]. Furthermore, certain experiments have been conducted on the formation of a notch (a cut induced by so called wave action) in soil and clay coastal slopes [1]. The objective of this study is to investigate the influence of a different loading field and different initial opening on the propagation of secondary cracks, using an XFEM based LEFM approach in ABAQUS and compare the results with those derived by theoretical method, LEFM.

4.1 INFLUENCE OF DIFFERENT LOADING FIELD ON THE DIRECTION OF THE SECONDARY CRACK PROPAGATION

As introduced in the motivation, the ratio of lateral pressure and vertical pressure differs when the loading history of the earth is different. It is supposed that direction of the secondary crack propagation is related to the ratio of stress intensity factors in different mode. Under mixed mode of I and II, the angle α with respect to the crack plane of the initial notch is proved to be affected by the ratio of K_{II}/K_I.

4.1.1 Extended Finite Element Method

4.1.1.1 Test formulation in ABAQUS

Three tests are conducted in this section, of which the ratios of normal and shear stress are more than one, equal to one, and less than one, respectively. The geometry of the slope (see Fig. 4.1.) is referred to the previous experimental study conducted by Luis E. Vallejo [39]. The thickness of the slope is 25.4 mm. The load condition in each test is identical and consists of vertical pressure on the top of the slope and horizontal displacement Δu on the right, shown in Fig. 4.2. Movement is restrained in all directions on the left, right and bottom face.

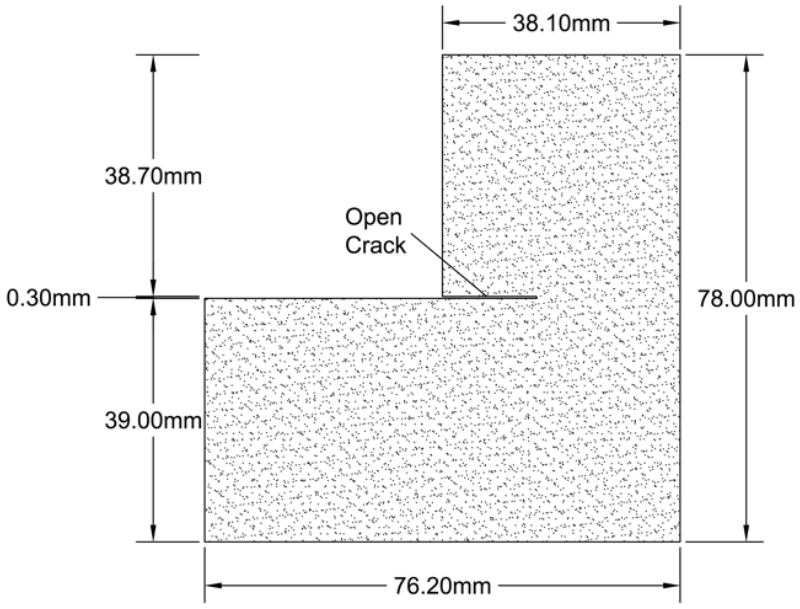

Figure 4.1. Dimension of slope with an open notch at its toe

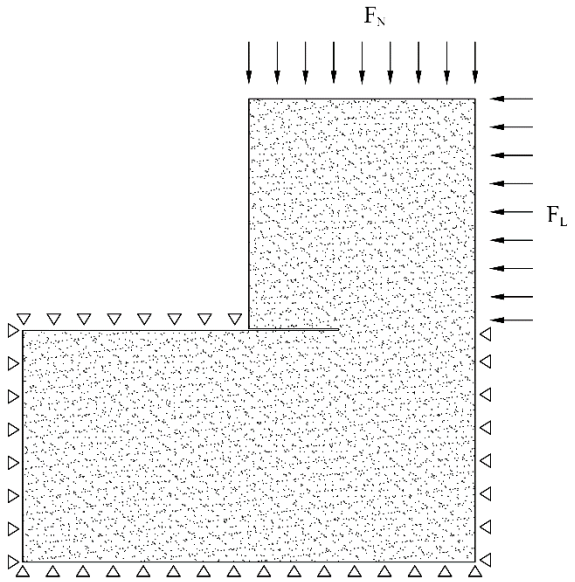

Figure 4.2. Load conditions comprising a normal force and a lateral force

The material properties, Young's Modulus and Poisson's ratio of slope are defined as same as in the uniaxial and biaxial test.

Only static analysis is allowed in XFEM in ABAQUS, hence, a general static step is selected. In addition, the step time is set to be 0.2 second with the minimum time increment as small as 10e-17 second so that the system is able to keep running. More importantly, because of enrichment of the approximation, the maximum number of attempts allowed for each iteration is larger than that in the standard finite element method. Consequently, the number of attempts, I_A increases to 30 instead of the default value 5.

In order to prevent the volume locking of the element, a CPS4R (free four-node bilinear) element is selected. Because that the real test is conducted on the so called plane stress direct shear apparatus (PSDSA), the plane stress element is selected.

4.1.1.2 Fracture criterion utilized in ABAQUS

The maximum principal stress fracture criterion is selected to identify the crack initiation, and the maximum principal stress is set to be the tensile strength of the normal clay. A proper damage distance is selected in order to terminate the test. The crack propagation is identified using LEFM based on the extended finite element method in ABAQUS. The direction of the crack is set to be normal to the maximum tangential stress around a crack tip.

4.1.1.3 Result analysis

The process of the crack initiation and propagation in each condition simulated in ABAQUS are shown in Fig. 4.1- 4.3.

The comparisons of the final crack are shown in Fig. 4.6. In order to clearly observe the direction of the final crack propagation, another drawing was created based on the export result of ABAUQS, shown in Fig. 4.7.

It is supposed that the lateral force F_L induced from the horizontal displacement is also identical for each test considering

$$F_L = EA\frac{\Delta u}{L} \tag{4.1}$$

where the magnitude of each term on the right of the equation is identical in each test, denoting E with the Young's modulus of the material, A the area of the loading area on the right face, L the vertical length of the loading area. In order to derive the lateral force, the reaction force of each node on the segment of the lateral load is exported and summed in the final stress contour of each test.

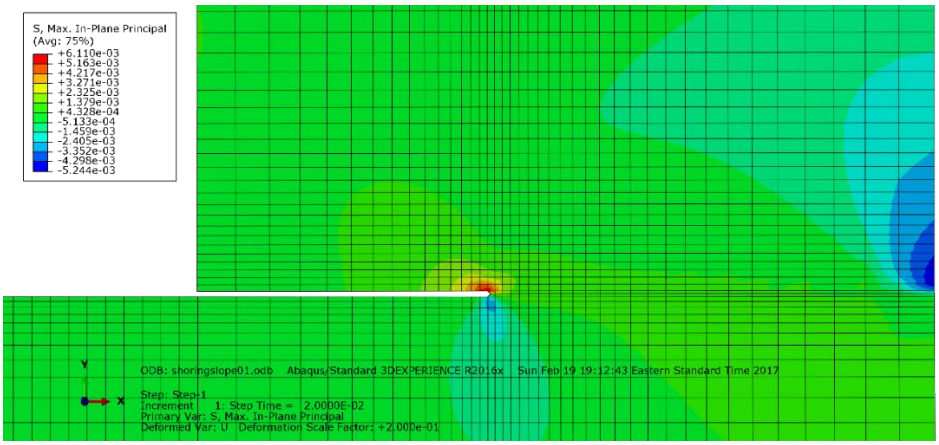

(a) in the beginning

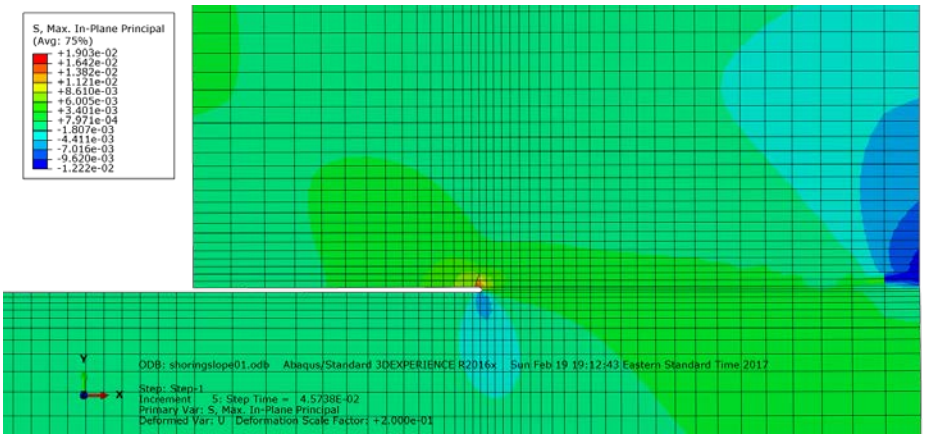

(b) when the crack initiates

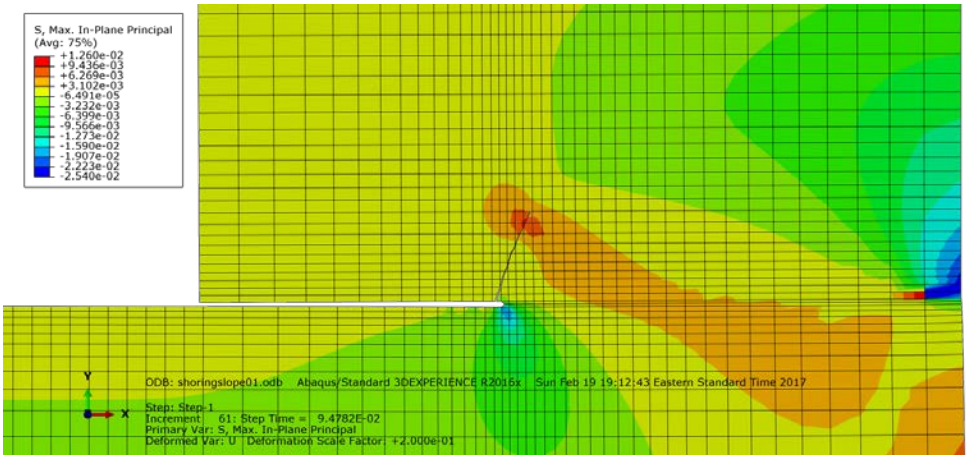

(c) after the crack propagates

Figure 4.3. Maximum principal stress contour (a) in the beginning (b) when the crack initiates (c) after the crack propagates for the case in which $\tau/\sigma_n > 1$

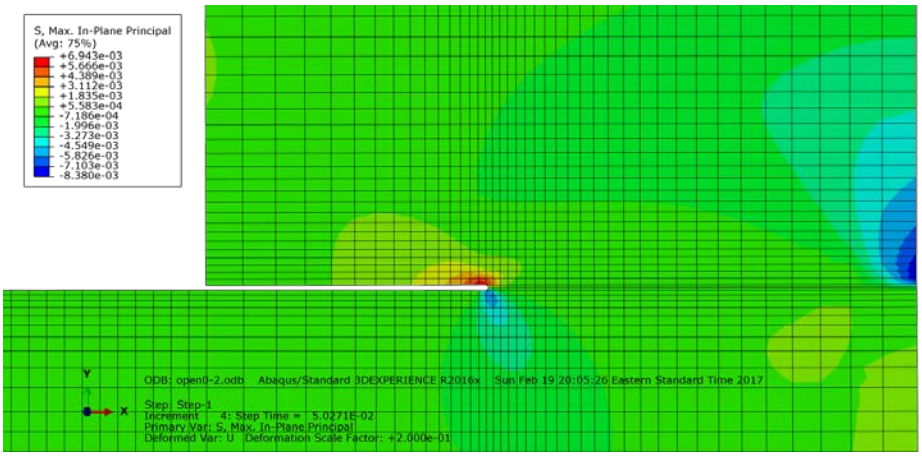

(a) in the beginning

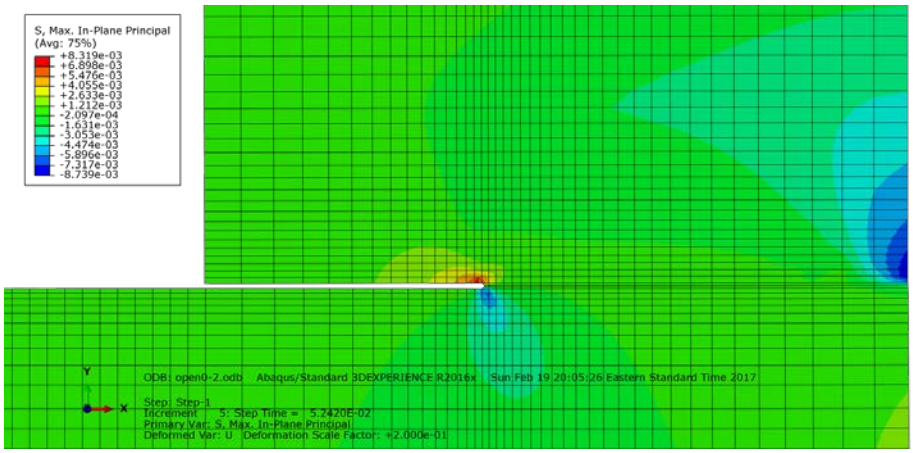

(b) when the crack initiates

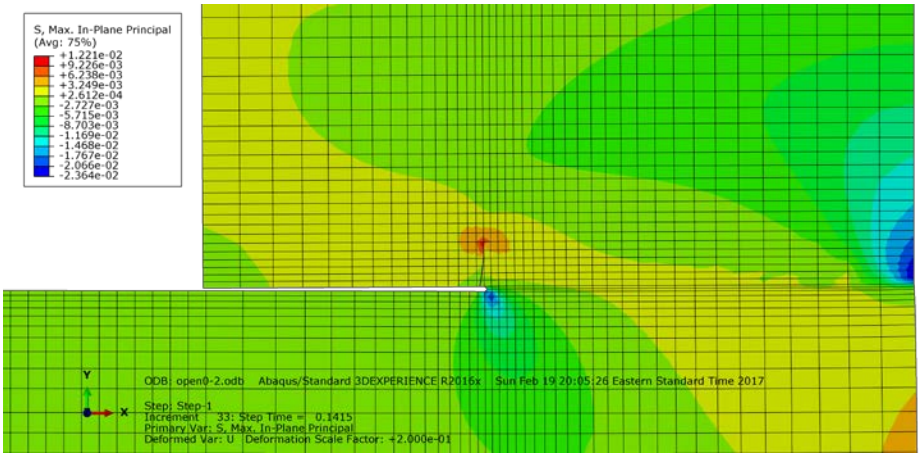

(c) after the crack propagates

Figure 4.4. Maximum principal stress contour (a) in the beginning (b) when the crack initiates (c) after the crack propagates for the case in which $\tau/\sigma_n \approx 1$

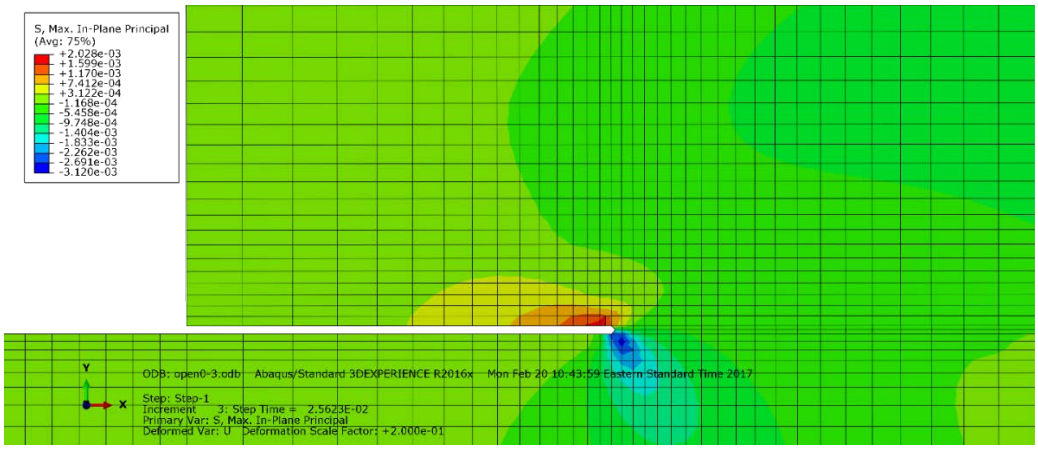

(a) in the beginning

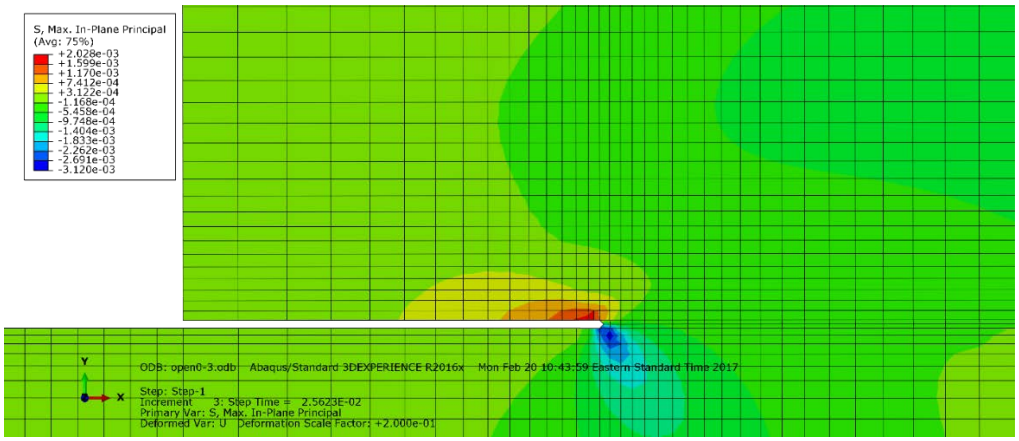

(b) when the crack initiates

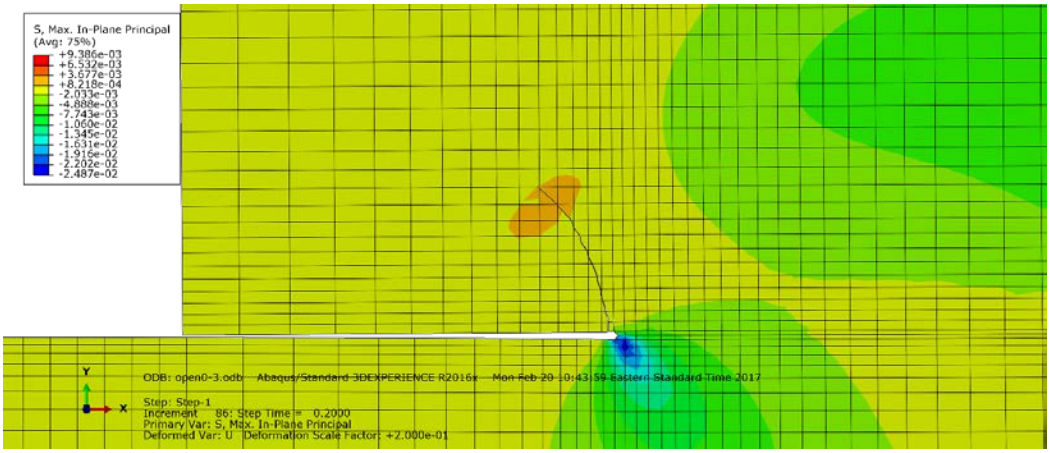

(c) after the crack propagates

Figure 4.5. Maximum principal stress contour (a) in the beginning (b) when the crack initiates (c) after the crack propagates for the case in which $\tau/\sigma_n < 1$

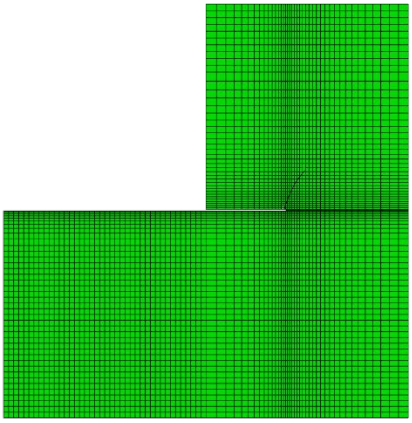

(a) $\tau/\sigma_n > 1$

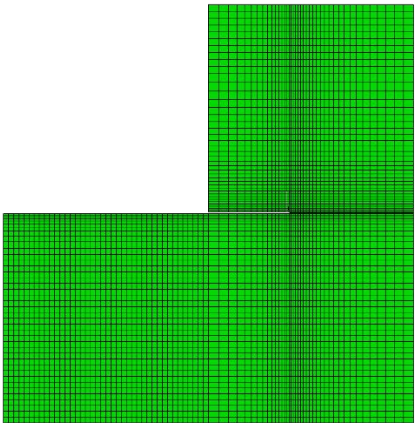

(b) $\tau/\sigma_n \approx 1$

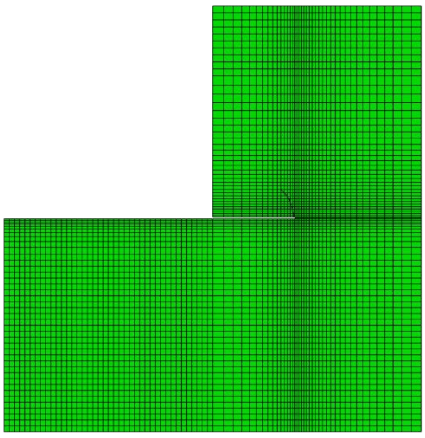

(c) $\tau/\sigma_n < 1$

Figure 4.6. Final step with the angle of crack propagation in three tests (a) $\tau/\sigma_n < 1$; (b) $\tau/\sigma_n \approx 1$; (c) $\tau/\sigma_n < 1$

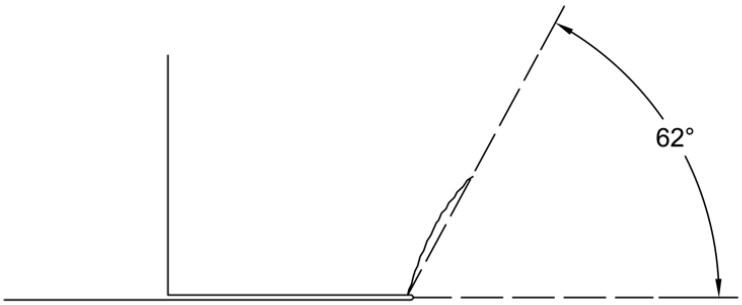

(a) $\tau/\sigma_n > 1$

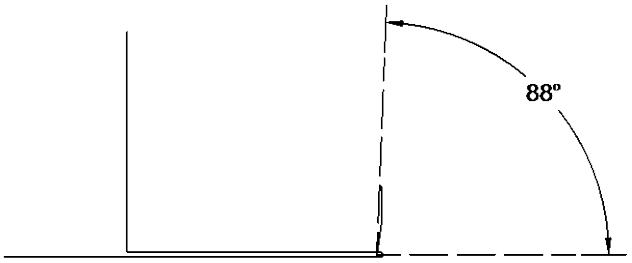

(b) $\tau/\sigma_n \approx 1$

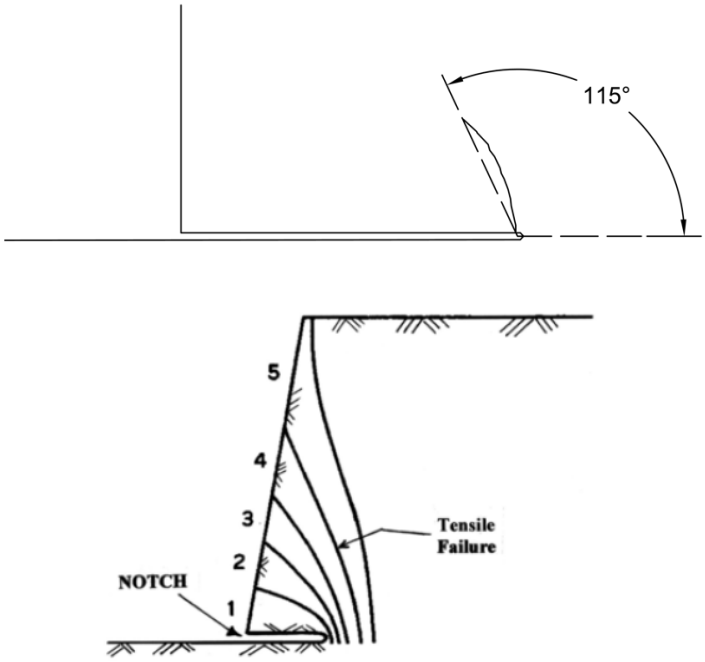

(c) $\tau/\sigma_n < 1$ and the slope of real case in Mississipi [1]

Figure 4.7. Final step with the angle of crack propagation in three tests (a) $\tau/\sigma_n < 1$; (b) $\tau/\sigma_n \approx 1$; (c) $\tau/\sigma_n < 1$

4.1.2 Linear elastic fracture mechanics approach

Given P_N the vertical pressure on the top, P_L the lateral pressure resulted from the uniform displacement on the right, and A1, A2 the area of the total and half of the top and the right face of the slope, respectively, the induced normal stress, σ_n and shear stress, τ acting on the initial crack planes is derived as

$$\sigma_n = P_N$$
$$\tau = \frac{F_L}{A_2} = P_L \tag{4.2}$$

The vertical pressure and the exported lateral pressure in each condition are shown in Table. 4.1.

Theoretical analysis was carried out on the basis of the same load condition in XFEM analysis in order to compare the results of the two methodologies.

Table 4.1. Vertical pressure and lateral pressure acting on the slope

	open0-1	open0-2	open0-3
F_L, N	12.63	7.59	5.10
Loading Area,mm^2	990.60	990.60	990.60
τ, MPa	0.01	0.01	0.01
σ, MPa	0.01	0.01	0.02
σ/τ	1.82	1.09	0.34

According to the maximum tangential stress criterion in LEFM theory given by Erogan and Sih [16], the angle of the secondary crack is determined by

$$\sin\alpha + \frac{K_{II}}{K_I}(3\cos\alpha - 1) = 0 \tag{4.3}$$

where

$$K_{\mathrm{I}} = 1.1215\ \sigma_n(\pi c)^{1/2}$$
$$K_{\mathrm{II}} = 1.1215\ \tau\ (\pi c)^{1/2} \tag{4.4}$$

Substituting Eq. 4.4 into Eq. 4.3, we obtain

$$\sin\alpha + \frac{\tau}{\sigma_n}(3\cos\alpha - 1) = 0 \tag{4.5}$$

The resulting analytical solution derived using the theoretical method described above is shown in Table 4.2.

Table 4.2. Theoretical solutions of α, the angle of crack propagation with respect to the crack plane

	open0-1	open0-2	open0-3
τ/σ_n	1.82	1.09	0.34
α, degree	80.5	88.46	120.72

4.1.3 Comparison between XFEM and LEFM Approach

Defined with $\mathrm{t} = \tau/\sigma_n$, the equation on the above can now be rewritten as

$$\sin\alpha + \mathrm{t}(3\cos\alpha - 1) = 0 \tag{4.6}$$

The angle of propagation is plotted against the ratio of shear to normal stress, as shown in Fig. 4.8.

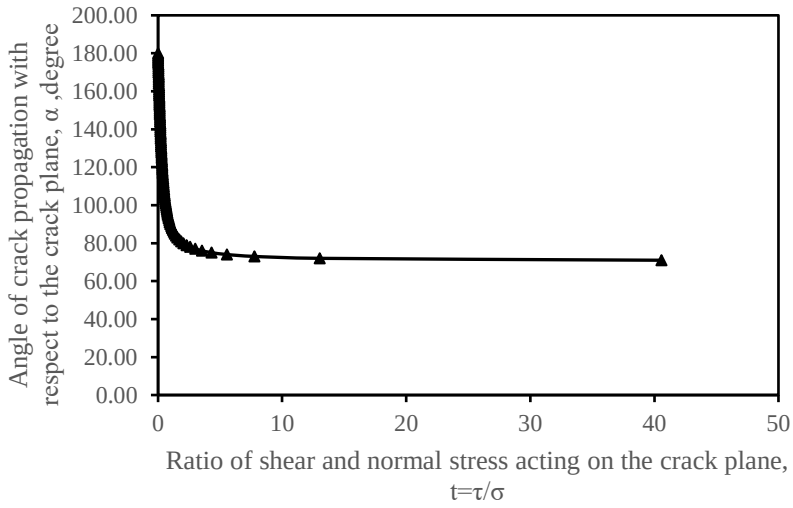

Figure 4.8. Crack propagation angle, α plotted against the ratio of shear and normal stress, t derived with theoretical method

The results of the XFEM and LEFM approach used in this study are combined in Table 4.3. and compared in Fig. 4.9.

As shown in Fig. 4.9, two methods give the similar solution in terms of the case in which ratio of shear and normal stress equals to one and similar results are obtained when the ratio is less than one. When the ratio exceeds one, XFEM cannot simulate the same angle as theoretical method. In general, simulation of arbitrary crack propagation based on XFEM is closer to the theoretical solution when the normal stress is larger than the shear stress acting on the crack plane.

The two methods prove that a crack will propagate at a right angle with respect to the crack plane when the shear stress is equal to normal stress, at an acute angle when shear is greater than normal stress, and at an obtuse angle when shear is less than normal stress. In addition, the angle of the secondary crack propagation decreases as the ratio of shear to normal stress increases. It is not difficult to comprehend that when the shear stress is acting on the top of the crack plane (Mode

II), the tension will be induced above the crack tip on the right so that the crack will extend to the right, as shown in Fig. 4.10.

Table 4.3. Theoretical and numerical solutions to the angle of propagation under different ratio of shear and normal stress

	open0-1	open0-2	open0-3
$t=\tau/\sigma$	1.82	1.09	0.34
theoretical α, degree	80.50	88.46	120.72
numerical α, degree	62.00	88.00	115.00

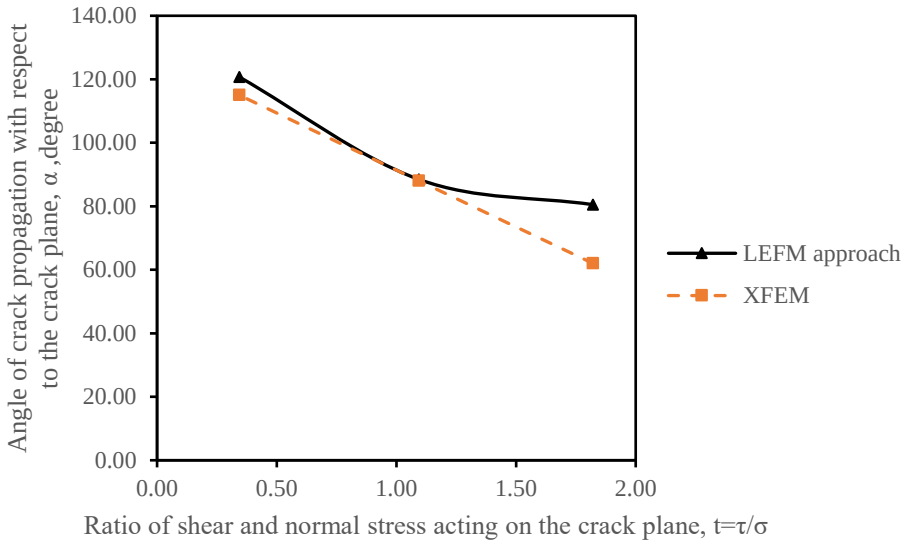

Figure 4.9. Comparison between theoretical and numerical solutions of angle of crack propagation

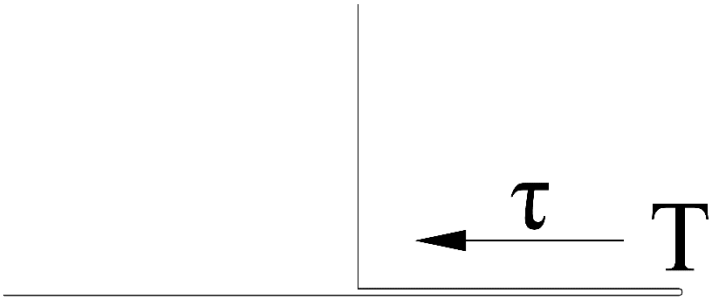

Figure 4.10. Stress field around the crack tip under the shear stress

4.2 INFLUENCE OF DIFFERENT OPENING OF INITIAL CRACK ON THE DIRECTION OF THE SECONDARY CRACK PROPAGATION

When there is a notch at the toe of a coastal slope, wave impact and abrasion will cause erosion and the notch will grow. This section investigates how the increasing degree of the opening influences the secondary crack propagation. The theoretical solution introduced above focuses on the horizontal notch, a transformation of the force is needed for the inclined crack plane to adapt the method.

4.2.1 Extended finite element method

4.2.1.1 Test formulation

In order to explore how the degree of opening of notch influences the direction of crack propagation, the load conditions were set to be same. Considering the result from the last section, i.e., that XFEM produces a better simulation when the shear stress is less than normal stress, the

ratio of shear to normal stress was set to be 0.82 in this section. The only variation, the angle of the initial crack for each of the three tests were 0 degree, 30 degree, and 45 degree, respectively. One of the benefits of partition is that the change in the angle only affects the region at the crack tip, thus, a large amount of time was saved when modifying the mesh configuration.

4.2.1.2 Result analysis

The same methodology was adapted to derive the lateral force, F_L from the node reaction force. It is not difficult to comprehend that the lateral force at the final step was same in each test when the lateral distance was set to be identical for all three. However, the lateral force was expected to differ when the crack initiated. The resulting lateral force at initiation of the crack is shown in Table 4.4 and plotted in Fig. 4.11 with respect to the opening of notch. Calculations of the normal and shear stress acting on the crack plane are also indicated in Table 4.4.

As indicated in Fig. 4.11, the lateral force increases as the initial opening increases, that is, a slope with a notch of a larger degree of opening at the toe can resist a larger lateral force when the secondary crack initiates, which is consistent with the principle discussed in Chapter 2.

Table 4.4. Lateral force at crack initiation and final step for initial cracks with different degrees of opening

	open0-1	open0-2	open0-3
Initiation F_L, N	1.06	1.90	5.05
Final step F_L, N	10.60	10.60	10.60
τ, MPa	0.01	0.01	0.01
σ_n, MPa	0.013	0.013	0.013
τ/σ_n	0.82	0.82	0.82

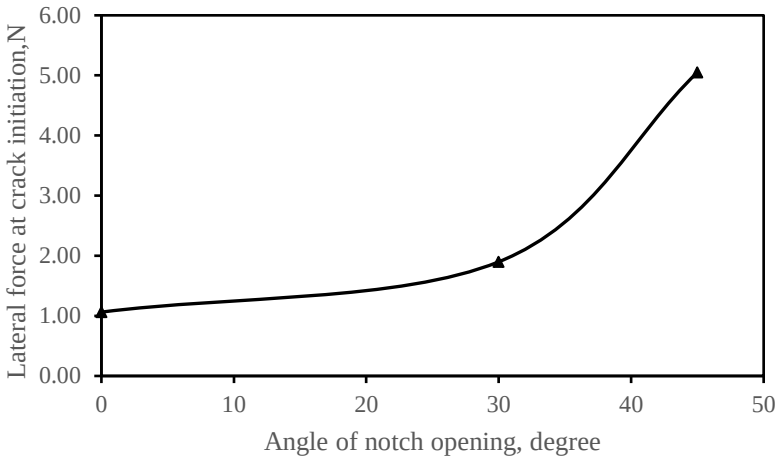

Figure 4.11. Lateral force at initiation of the secondary crack plotted against different degree of opening

The process of the crack initiation and propagation in each condition simulated in ABAQUS are shown in Fig. 4.12- 4.14.

In order to clearly observe the direction of the final crack propagation, another drawing is conducted based on the export result of ABAUQS, shown in Fig. 4.15.

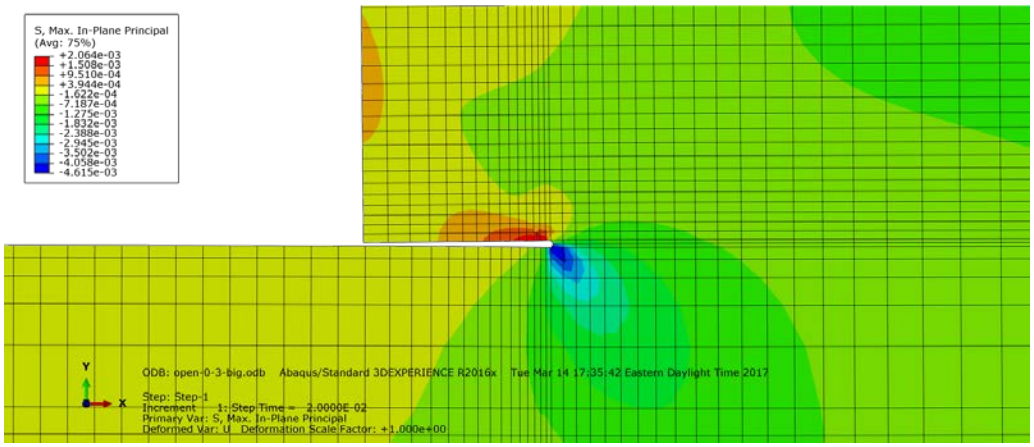

(a) when the crack initiates

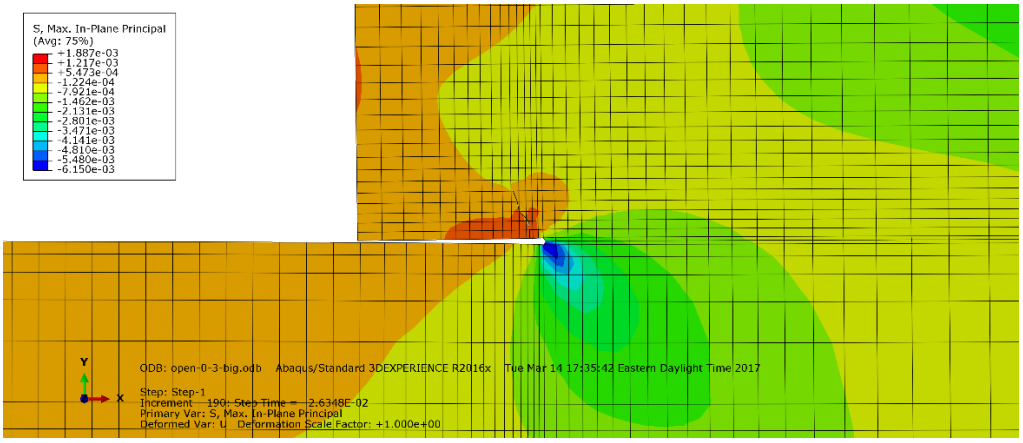

(b) after the crack propagates

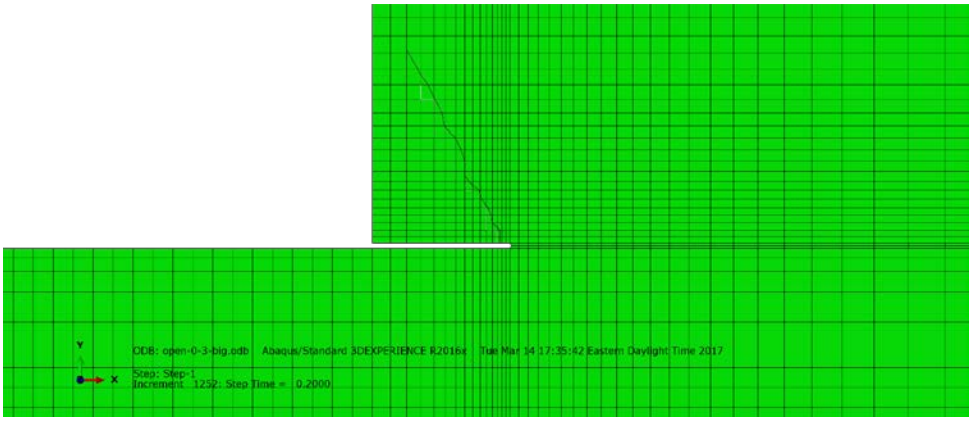

(c) Geometry of the crack propagation at the final step

Figure 4.12. Maximum principal stress contour (a) when the crack initiates; (b) after the crack propagates and (c) geometry of the final crack propagation when the initial crack opening is 0 degree

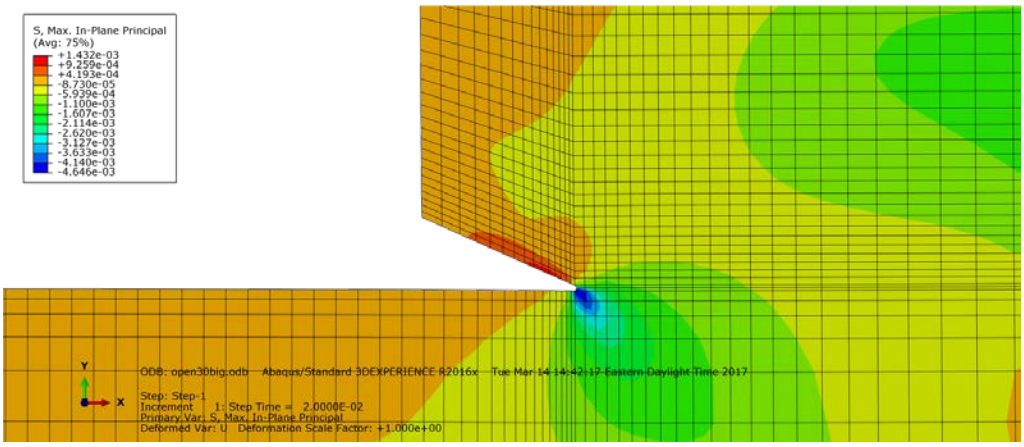

(a) when the crack initiates

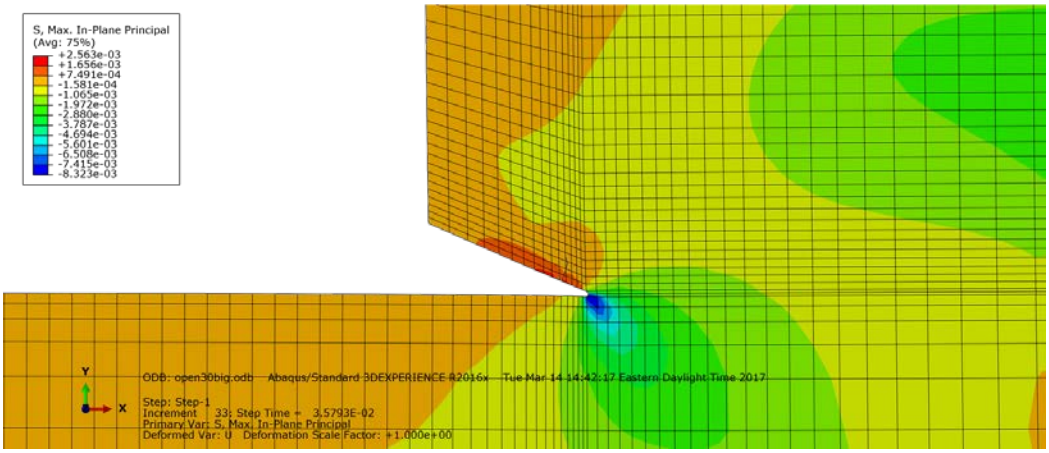

(b) after the crack propagates

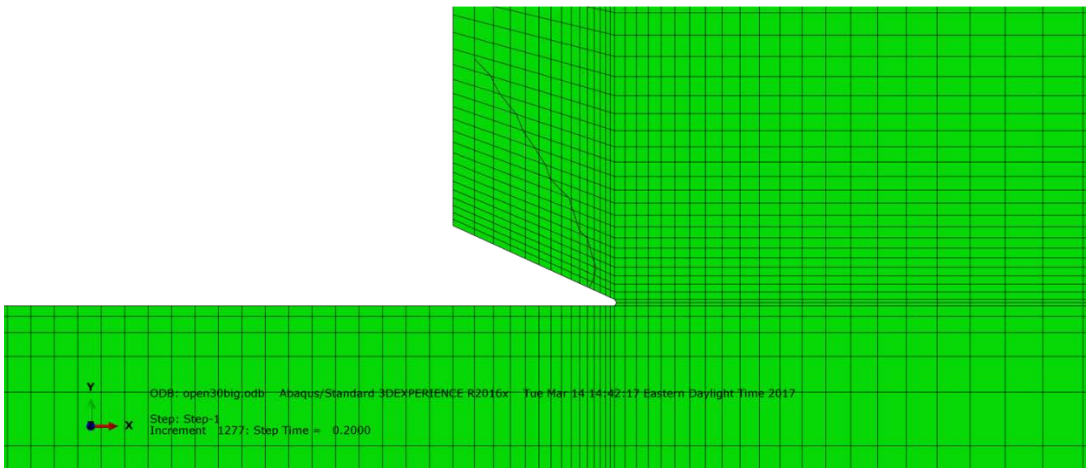

c) Geometry of the crack propagation at the final step

Figure 4.13. Maximum principal stress contour a) when the crack initiates; b) after the crack propagates and c) geometry of the final crack propagation when the initial crack opening is 30 degree

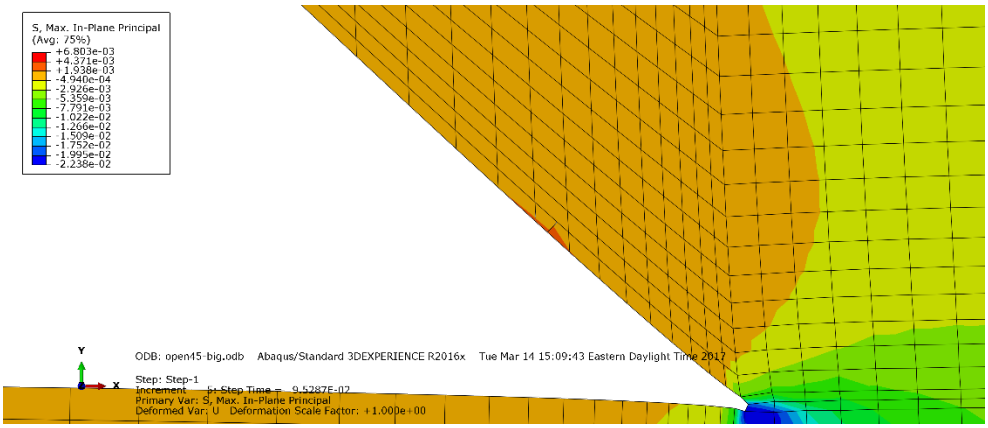

(a) when the crack initiates

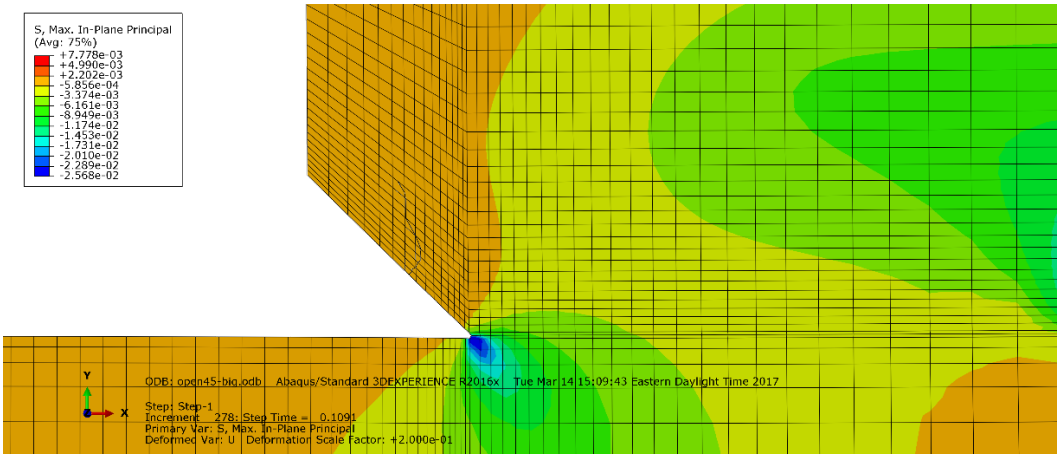

(b) after the crack propagates

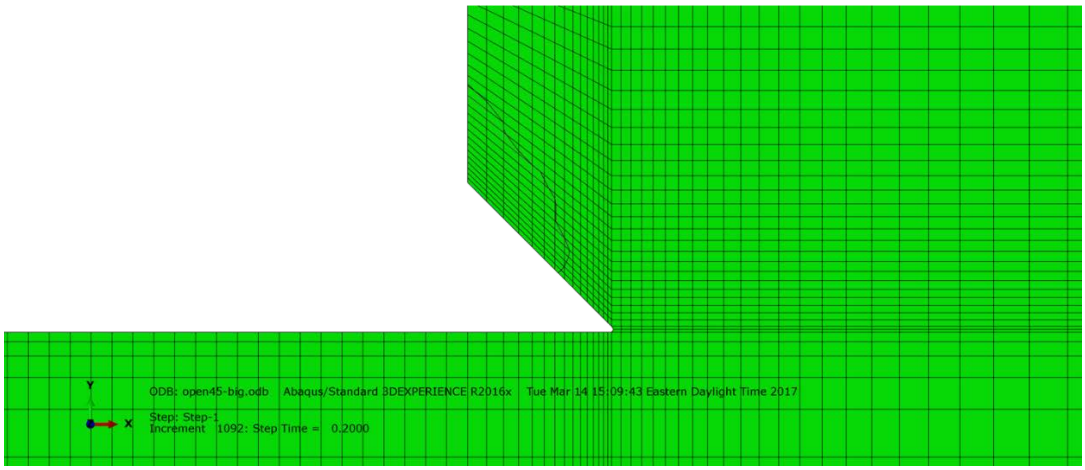

c) Geometry of the crack propagation at the final step

Figure 4.14. Maximum principal stress contour (a) when the crack initiates; (b) after the crack propagates and c) geometry of the final crack propagation when the initial crack opening is 30 degree

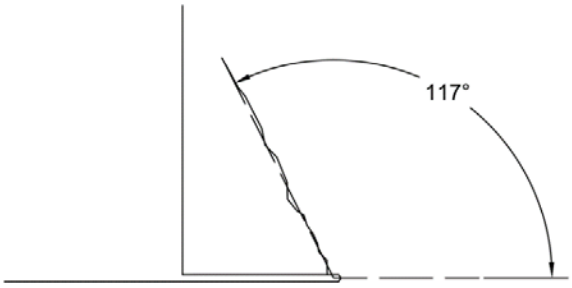

(a) Original crack opening, $\beta = 0°$

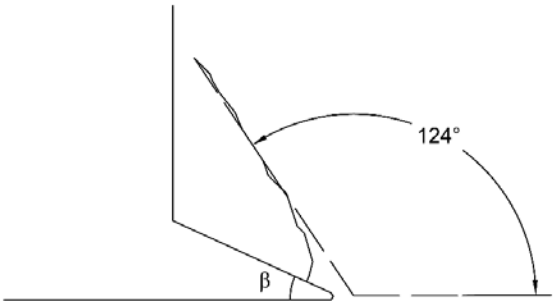

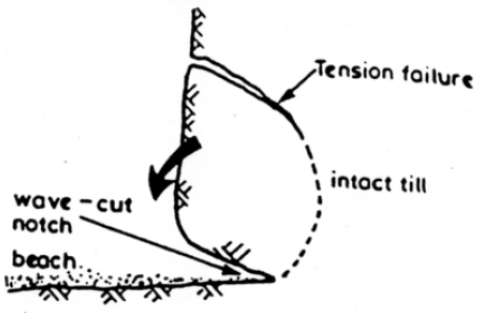

(b) Original crack opening, $\beta = 30°$ and the corresponding coastal slope in England [1]

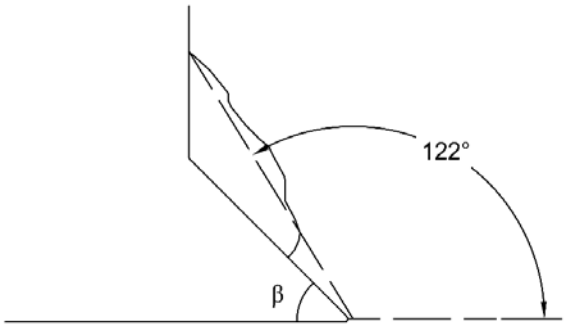

(c) Original crack opening, $\beta = 45°$

Figure 4.15. Final step with the angle of crack propagation in three test (a) Original crack opening, $\beta = 0°$; (b) Original crack opening, $\beta = 30°$; (c) Original crack opening, $\beta = 45°$

The angle of the secondary crack propagation is defined as the angle between the final crack propagation and the crack plane. The entire crack is considered to have three components, the crack initiation, the crack growth, and the crack propagation. For the case of original crack opening, β is equal to 30 degree and 45 degree, the crack growth part is more obvious than in the standard notch. In these two cases, variation of the crack plane is taken into consideration. For the standard notch with zero opening, the crack plane is horizontal; however, if the initial crack has an angle of β, then the crack plane is defined as the angular bisector of the two crack faces. Hence, the final crack propagation angle, α' should be the same as the angle shown in the drawing, α plus $\beta/2$, shown in Table 4.5.

Table 4.5. Numerical solutions for the angle of secondary propagation with respect to the crack plane

	Open0	Open30	Open45
β, degree	0	30	45
α, degree	117.00	124.00	122.00
α', degree	117.00	139.00	144.50

4.2.2 Linear elastic fracture mechanics approach

Theoretical solutions from Erdogan and Sih [16] are applicable for the standard notch, however, for the case in which the notch has an initial angle, the solution should be modified and extended by using the load resolution. Denoted with σ_n the normal stress on the standard notch, τ the shear stress on the standard notch, the normal stress σ_n' and shear stress τ' of the notch with an initial angle β can be derived as

$$\begin{aligned} \sigma_n' &= \sigma_{n2} + \tau_1 \\ &= \sigma_n \cos\beta + \tau \sin\beta \\ \tau' &= \tau_2 - \sigma_{n1} \\ &= \tau \cos\beta - \sigma_n \sin\beta \end{aligned} \tag{4.7}$$

where σ_{n2} and σ_{n1} are the components of σ_n parallel and perpendicular, respectively, to the crack face, and τ_1 and τ_2 are the components of τ perpendicular and parallel to the crack face respectively, as shown in Fig. 4.16.

The ratio of the shear and normal stress, t' for the notch with an initial angle is presented as

$$\begin{aligned} t' &= \frac{\tau'}{\sigma_n{}'} = \frac{\tau\cos\beta - \sigma_n \sin\beta}{\sigma_n \cos\beta + \tau \sin\beta} \\ t' &= \frac{t - \tan\beta}{1 + t\tan\beta} \end{aligned} \tag{4.8}$$

where $t = \tau/\sigma_n$.

Now we can derive the direction equation for the notch with an initial angle as

$$\sin\alpha + t'(3\cos\alpha - 1) = 0 \tag{4.9}$$

where

$$t' = \frac{t - \tan\beta}{1 + t\tan\beta} \tag{4.10}$$

As seen in the equation above, if β increases, t' will decrease, and based on the graph of the direction equation, the angle for the crack propagation will increase. In other words, a larger angle of the secondary crack propagation will be induced if given a notch with a larger initial angle.

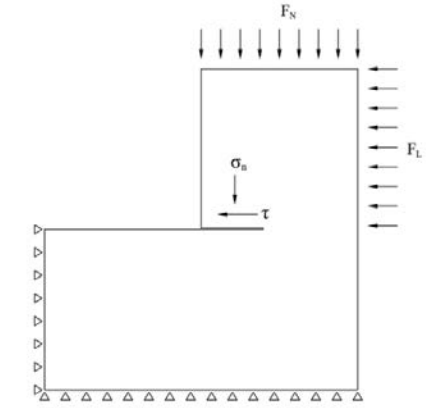

(a)

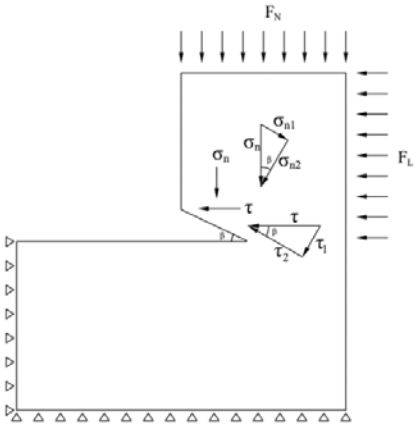

(b)

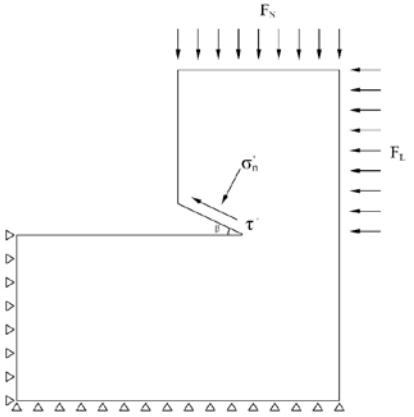

(c)

Figure 4.16. Load transformation from the normal notch to the notch with an angle β

(a) normal and shear stress acting on the normal notch; (b) load resolution of the normal and shear stress;

(c) resulted normal and shear stress on a notch with an angle

Theoretical solutions for the directions of crack propagation for each geometry of notch are shown in Table. 4.6.

Table 4.6. Theoretical result for the angle of secondary crack propagation given different initial openings

	Open0	Open30	Open45
β, degree	0	30	45
t'	0.82	0.16	0.10
α, degree	94.18	144.10	157.00

4.2.3 Comparison between XFEM and LEFM approach

The secondary crack propagation angle, α from the numerical and theoretical methods are compared in Table 4.7 and plotted with respect to the actual ratio of shear and normal stress, t and the degree of opening notch, β in Fig. 4.17 (a) and (b), respectively.

Table 4.7. Results of angle, β of secondary crack propagation for different angles of notch from numerical and theoretical method

	Open0	Open30	Open45
β	0	30	45
t'	0.82	0.16	0.10
theoretical α, degree	94.18	124.10	157.00
numerical α, degree	117.00	139.00	144.50

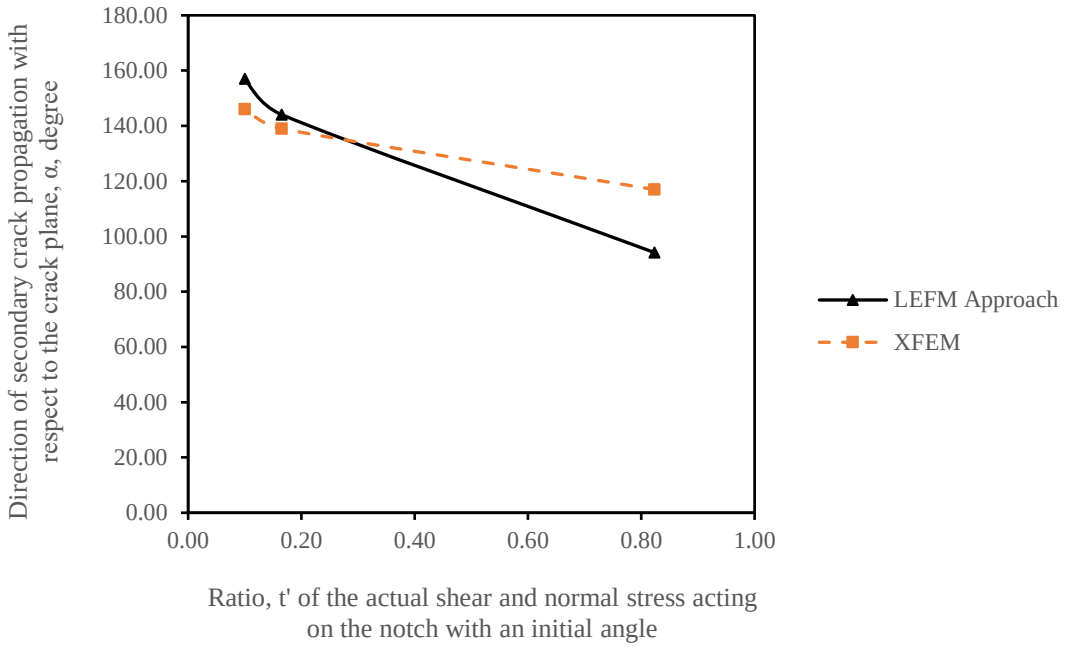

(a)

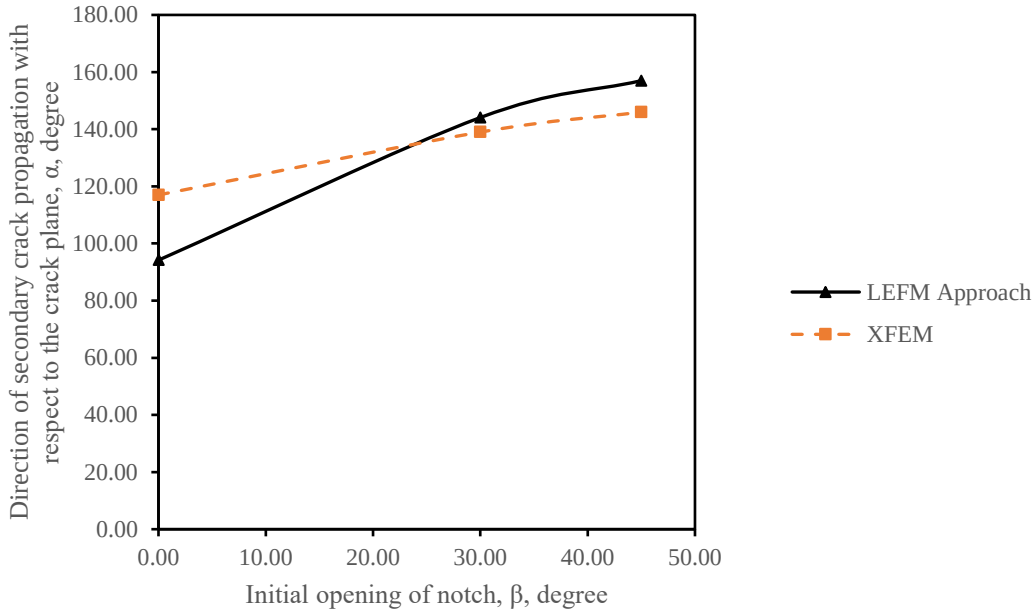

(b)

Figure 4.17. Comparison between theoretical and numerical approaches with regard to the angle of the secondary crack propagation against (a) the actual ratio of shear and normal stress on the crack plane and (b) different openings of the notch

As shown in Fig. 4.17, the theoretical and numerical method indicate that the angle of the secondary crack propagation with respect to the crack plane grows when the opening of the notch increases. This can be observed by that the actual ratio of shear and normal stress acting on the crack plane decreases when the opening of notch grows.

In addition, the results derived from the two method are more similar when the ratio of shear and normal is lower. In another words, a lower ratio of shear to normal stress, or a larger initial opening of the notch will increase the accuracy of XFEM simulation. However, at the narrow notch, the difference between the two method is larger. Mesh contour is not so precise at the concentration with small degree of opening which causes the difference with LEFM.

The results also indicates that although XFEM based LEFM approach in ABAQUS is applicable for mixed mode, this method produces more accurate results when simulating the crack propagation under the load condition of Mode I than that under Mode II. The method associated with Mode I more accurately simulates the secondary propagation under mixed loading.

5.0 CONCLUSIONS

This study of clay under uniaxial compression and direct shear test, using both numerical analysis based on the finite element method as well as theoretical analysis using linear elastic fracture mechanics produced the following conclusions:

1. The geometry of the opening in clay significantly influences both the maximum stress around the excavation boundary as well as the secondary propagation at the notch of a slope. In uniaxial compression tests on clay with excavation, compression at the crack with larger degree of opening produces a lower value in the boundary excavation. However, the magnitude of tension varies a little in terms of different degree of opening. In direct shear test, both tension and compression reach the lowest value when H/W equals one. In the direct shear test for the slope with a notch at its toe, the angle of the secondary crack propagation increases as the degree of initial opening grows. In addition, the ratio of shear stress to normal stress also influences the secondary crack propagation. With more shear stress acting on the slope, the crack will propagate to the right side of the crack tip.
2. In simulating the uniaxial compression test on clay with excavation of different geometry, FEM produces better results for modeling maximum compression and tension around the excavation boundary at the concentrations with a larger curvature, whereas at concentrations with a narrow opening, the results are not so accurate. In modeling the direct shear test, the compression results more closely resembled the theoretical results than the tension results. In

modelling the arbitrary crack propagation at the notch of a slope, the XFEM based LEFM method in ABAQUS accurately determines the angle of propagation accurately under mixed modes of loading. However, the results are not so accurate when the Mode II contributes a larger part in the load condition. The results from XFEM are closer to the results from LEFM when the initial opening of the notch is smaller for the reason that the actual ratio of shear and normal stress acting on the crack plane grows as the initial opening increases.

3. LEFM is utilized successfully to solve the traditional problem as well as the problem with extended situations. For the uniaxial compression test, the LEFM is adapted directly. For the direct shear test, the loading system is modified to that in the theoretical problem, which has been effective in giving the reasonable results. For the slope with a notch at its toe, maximum tangential stress criterion is extended to the case with an inclined crack plane. However, some limitations are found in using the theoretical solutions.
4. The author provides an explanation for the difference between XFEM and LEFM in simulating the tension behavior of brittle material under direct shear stress field in this study, however, more research is needed to investigate why this difference only occurs in tension behavior but not in compression behavior.
5. This study provides only one real-world case that matched the simulation (ratio t is more than one). In future study, it would be beneficial to find and discuss additional practical cases related to the other two simulations as well.

BIBLIOGRAPHY

[1] Vallejo, Luis E. "The Influence of Open and Closed Toe Notches on the Stability of Rock and Soil Slopes." Integrating Innovations of Rock Mechanics: Proceedings of the 8th South American Congress on Rock Mechanics, 15–18 November 2015, Buenos Aires, Argentina. IOS Press, 2015.

[2] Lutton, R. J. *FRACTURES AND FAILURE MECHANICS IN LOESS AND APPLICATIONS TO ROCK MECHANICS*. No. AEWES-RR-S-69-1. ARMY ENGINEER WATERWAYS EXPERIMENT STATION VICKSBURG MISS, 1969.

[3] Hutchinson, John Neville. *Cliffs and shores in cohesive materials: geotechnical and engineering geological aspects*. publisher not identified, 1986.

[4] Hutchinson, J. N. "General report: morphological and geotechnical parameters of landslides in relation to geology and hydrogeology: Proc 5th International Symposium on Landslides, Lausanne, 10–15 July 1988V1, P3–35. Publ Rotterdam: AA Balkema, 1988." *International Journal of Rock Mechanics and Mining Sciences & Geomechanics Abstracts*. Vol. 26. No. 2. Pergamon, 1989.

[5] Griffith, A. A. "The phenomena of rupture and flow in solids." Philosophical transactions of the royal society of London. Series A, containing papers of a mathematical or physical character 221 (1921): 163-198.

[6] Griffith, A. A. "The theory of rupture." Proceedings of the 1st Int. Congress on Applied Mechanics, Delft. 1924.

[7] Irwin, George R. "Analysis of stresses and strains near the end of a crack traversing a plate." Spie Milestone series MS 137.167-170 (1997): 16.

[8] Irwin, G. R., J. A. Kies, and H. L. Smith. "Fracture strengths relative to onset and arrest of crack propagation." Proc. ASTM. Vol. 58. 1958.

[9] Rice, James R. "A path independent integral and the approximate analysis of strain concentration by notches and cracks." ASME, 1968.

[10] Bazant, Zdenek P., and Jaime Planas. *Fracture and size effect in concrete and other quasibrittle materials*. Vol. 16. CRC press, 1997.

[11] Kirsch, G. "Theory of Elasticity and Application in Strength of Materials." Z. des Ver. Dtsch. Ing 42.29 (1898): 797-807.

[12] Jaeger, John Conrad, Neville GW Cook, and Robert Zimmerman. Fundamentals of rock mechanics. John Wiley & Sons, 2009.

[13] Brown, Edwin T., and Barry HG Brady. Rock mechanics: for underground mining. George Allen, 1985.

[14] Poulos, Harry George, and Edward Hughesdon Davis. Elastic solutions for soil and rock mechanics. John Wiley, 1974.

[15] Heok, E., and J. W. Bray. "Rock slope engineering." The Institution of Mining and Metallurgy, London (1977): 127-149.

[16] Erdogan, Fazil, and G. C. Sih. "On the crack extension in plates under plane loading and transverse shear." Journal of basic engineering 85.4 (1963): 519-527.

[17] Vallejo, Luis E. "Application of fracture mechanics to soils: an overview." Fracture Mechanics Applied to Geotechnical Engineering:. ASCE, 1994.

[18] Ingraffea, Anthony R., and Francois E. Heuze. "Finite element models for rock fracture mechanics." International Journal for Numerical and Analytical Methods in Geomechanics 4.1 (1980): 25-43.

[19] Henshell, R. D., and K. G. Shaw. "Crack tip finite elements are unnecessary." International journal for numerical methods in engineering 9.3 (1975): 495-507.

[20] Benzley, S. E. "Representation of singularities with isoparametric finite elements." International Journal for Numerical Methods in Engineering 8.3 (1974): 537-545.

[21] Gifford, L. Nash, and Peter D. Hilton. "Stress intensity factors by enriched finite elements." Engineering Fracture Mechanics 10.3 (1978): 485-496.

[22] Vitek, V. "Plane strain stress intensity factors for branched cracks." International Journal of Fracture 13.4 (1977): 481-501.

[23] Obata, Makoto, Siavouche Nemat-Nasser, and Yoshiaki Goto. "Branched cracks in anisotropic elastic solids." Journal of applied mechanics 56.4 (1989): 858-864.

[24] Chen, Y. Z., and Norio Hasebe. "New integration scheme for the branch crack problem." Engineering Fracture Mechanics 52.5 (1995): 791-801.

[25] Newman Jr, J. C. "An improved method of collocation for the stress analysis of cracked plates with various shaped boundaries." (1971).

[26] Belytschko, Ted, Yun Yun Lu, and Lei Gu. "Element-free Galerkin methods." International journal for numerical methods in engineering 37.2 (1994): 229-256.

[27] Belytschko, Ted, et al. "Meshless methods: an overview and recent developments." Computer methods in applied mechanics and engineering 139.1-4 (1996): 3-47.

[28] Fleming, M., et al. "Enriched element-free Galerkin methods for crack tip fields." International journal for numerical methods in engineering 40.8 (1997): 1483-1504.

[29] Belytschko, Ted, and Tom Black. "Elastic crack growth in finite elements with minimal remeshing." International journal for numerical methods in engineering 45.5 (1999): 601-620.

[30] Dolbow, John Everett. An extended finite element method with discontinuous enrichment for applied mechanics. Northwestern university, 1999.

[31] Dolbow, John, Nicolas Moës, and Ted Belytschko. "Discontinuous enrichment in finite elements with a partition of unity method." Finite elements in analysis and design 36.3 (2000): 235-260.

[32] Dolbow, J. O. H. N., and Ted Belytschko. "A finite element method for crack growth without remeshing." International journal for numerical methods in engineering 46.1 (1999): 131-150.

[33] Sukumar, Natarajan, et al. "Extended finite element method for three-dimensional crack modelling." International Journal for Numerical Methods in Engineering 48.11 (2000): 1549-1570.

[34] Sukumar, Natarajan, and Ted Belytschko. "Arbitrary branched and intersecting cracks with the extended finite element method." Int. J. Numer. Meth. Eng 48 (2000): 1741-1760.

[35] Belytschko, Ted, et al. "Arbitrary discontinuities in finite elements." International Journal for Numerical Methods in Engineering 50.4 (2001): 993-1013.

[36] Belytschko, Ted, Robert Gracie, and Giulio Ventura. "A review of extended/generalized finite element methods for material modeling." Modelling and Simulation in Materials Science and Engineering 17.4 (2009): 043001.

[37] Vallejo, Luis E. "The brittle and ductile behavior of a material containing a crack under mixed-mode loading." The 28th US Symposium on Rock Mechanics (USRMS). American Rock Mechanics Association, 1987.

[38] Jing, Lanru, and J. A. Hudson. "Numerical methods in rock mechanics." International Journal of Rock Mechanics and Mining Sciences 39.4 (2002): 409-427.

[39] Vallejo, Luis E. "Application of fracture mechanics to soils: an overview." Fracture Mechanics Applied to Geotechnical Engineering: ASCE, 1994.

[40] Vallejo, L. E. "The influence of fissures in a stiff clay subjected to direct shear." Geotechnique 37.1 (1987): 69-82.

[41] Moayed, R. Ziaie, S. Tamassoki, and E. Izadi. "Numerical modeling of direct shear tests on sandy clay." *World Academy of Science, Engineering and Technology* 61 (2012): 1093-1097.